Electronic Supplementary Material (ESI) for Physical Chemistry Chemical Physics.
This journal is © the Owner Societies 2024

Supplementary Information: Contrasting the Stability, Octahedral Distortions and Optoelectronic Properties of 2D and 3D $MABX_3$ (B = Ge, Sn, Pb; X = Cl, Br, I) Perovskites.

João G. Danelon,[*,†] Ramiro M. Santos,[*,‡] Alexandre C. Dias,[*,¶,§] Juarez L. F. Da Silva,[*,‡] and Matheus P. Lima[*,†]

†*Department of Physics, Federal University of São Carlos,* 13565-905*, São Carlos, São Paulo, Brazil*

‡*São Carlos Institute of Chemistry, University of São Paulo, P.O. Box* 780*,* 13560-970*, São Carlos, São Paulo, Brazil*

¶*University of Brasília, Institute of Physics, Brasília* 70919-970*, DF, Brazil*

§*Previous address: São Carlos Institute of Chemistry, University of São Paulo, P.O. Box* 780*,* 13560-970*, São Carlos, São Paulo, Brazil*

E-mail: joaodanelon@gmail.com; ramiromarcelo2@gmail.com; alexandre.dias@unb.br; juarez_dasilva@iqsc.usp.br; mplima@df.ufscar.br

Contents

1 Introduction

This document contains additional results and techniques details to support the most important findings reported within the manuscript. This document is separated into the following sections listed below:

1. Selected PAW projectors: technical details;
2. Goldschmidt tolerance factor;
3. Computational convergence tests;
4. Lattice parameters and total energy;
5. Octahedral volumes, bond lengths, effective coordination number, and bond angles;
6. Bader charge and cohesive energies decomposed for its constituents;
7. Density of states;
8. Electronic bands calculations with and without spin-orbit coupling correction;
9. Band gap correction with HSE06 functional;
10. Absorption coefficient.

2 Selected PAW Projectors: Technical Details

Table S1 Most important information of the selected PAW projectors. Species, PAW-PBE projector name (Title), electronic valence distribution (Valence), number of valence electrons (Z_{val}) and maximum recommended cutoff energy (`ENMAX`) for all chemical species composing the investigated perovskites.

Species	Title	Valence	Z_{val}	`ENMAX` (eV)
H	H_GW 21Apr2008	$1s^1$	1	300.000
C	C_GW_new 19Mar2012	$2s^2 2p^2$	4	413.992
N	N_GW_new 19Mar2012	$2s^2 2p^3$	5	420.902
Cl	Cl_GW 19Mar2012	$3s^2 3p^5$	7	262.472
Ge	Ge_d_GW 19Mar2013	$3d^{10} 4s^2 4p^2$	14	375.434
Br	Br 20Mar2012	$4s^2 4p^5$	7	216.285
Sn	Sn_d_GW 15Mar2013	$4d^{10} 5s^2 5p^2$	14	260.066
I	I_GW 12Mar2012	$5s^2 5p^5$	7	175.647
Pb	Pb_d_GW 14Apr2014	$5p^{10} 5s^2 6s^2 6p^2$	16	237.809

3 Goldschmidt Tolerance Factor

The Goldschmidt tolerance factor is one of the most common structure stability measures considered while studying metal halide perovskites. It relates the ionic radii of the species involved, as the tolerance factor (t) is defined by:

$$t = \frac{r_A + r_X}{\sqrt{2}\times(r_B + r_X)} \ . \tag{1}$$

The tolerance factor is a measure of how the ionic species are arranged and specify the crystal structure of the material, *i.e.*, if $t > 1$, we have a hexagonal structure, whereas for $t < 0.8$, the material is described from an orthorrombic unit cell. The best optoelectronic properties for metal halide perovskites are, however, encountered for cubic structures that happen in the range $0.8 < t < 1$.

Table S2 Goldschmidt tolerance factors for 3D MABX_3 perovskites.

BX	t
GeCl	1.108
GeBr	1.086
GeI	1.055
SnCl	0.967
SnBr	0.954
SnI	0.936
PbCl	0.938
PbBr	0.927
PbI	0.912

On Table S2 we present the tolerance factors for the 3D MABX_3 perovskites calculated following Equation 1 and the ionic radii of MA^+,[1] Ge^{2+},[2] Sn^{2+},[3] Pb^{2+},[2] Cl^-,[4] Br^-,[4] and I^-,[1] as compiled by Hoefler et al.[5] From the results present in the table, we note that, excluding the germanium-based materials that are strongly affected by Jahn–Teller distortions, the tolerance factor for all the studied materials are within the desired range for cubic structures, $0.8 < t < 1$.

4 Computational Convergence Tests

We performed convergence tests to identify the appropriate **k**-mesh and cutoff energy (`ENCUT`) using as test subject the 3D $MAPbI_3$ 1×1×1 and the 2D $(BA)_2(MA)Pb_2I_7$ compounds. Figure S1 shows a ball-and-stick representation of both 3D 1×1×1, panel (a), and 2D, panel (b), perovskites, where the original structures were obtained for both PbI-based configurations with the layered one being an experimental result of the work of Stoumpos et al.[6]

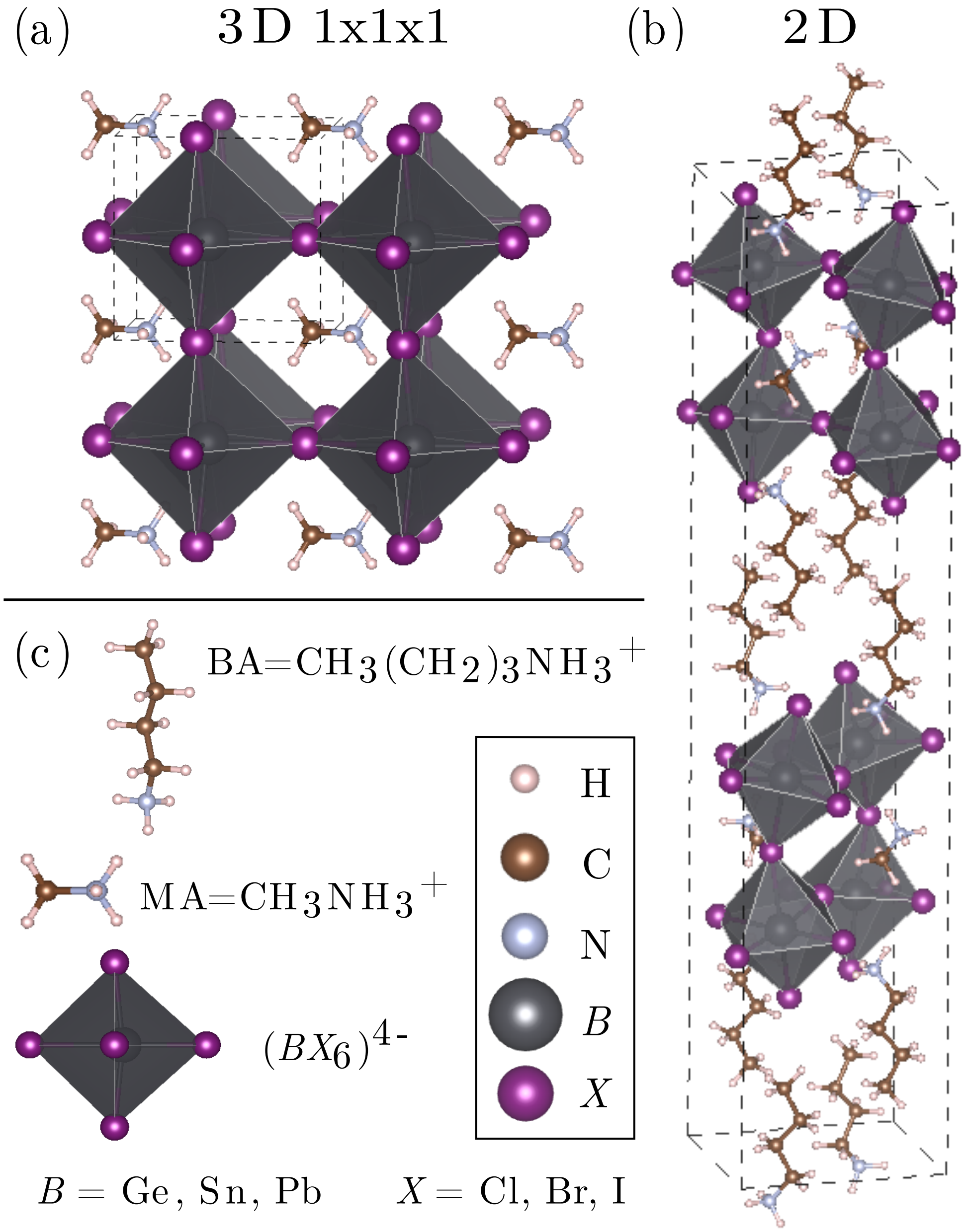

Figure S1 Crystal structures for 3D $1\times1\times1$ $MAPbI_3$ (a) and 2D $(BA)_2(MA)Pb_2I_7$ (b) perovskites. Panel (c) indicates the legend for the chemical species and structures, while the dashed lines indicate the unit cells.

We are aware of unrealistic descriptions while considering a $1\times1\times1$ unit cell compared to experimental results,[7] but we are able to perform convergence tests, take these results and then apply to supercell structures such as a 2×2×2 which will be investigated. This methodology is possible because the **k**-points test takes into account the characteristics of electronic states, which are not changed when considering supercells. Furthermore, the cutoff energy test depends on the chemical species and structure characteristics, which also do not vary when using a 2×2×2 structure.

4.1 k-mesh Convergence Test

For the **k**-mesh convergence, we fixed `ENCUT` $= 2 \times$ `ENMAX`$_{max}$ and varied the **k**-density between 5 and 45 Å^{-3} by scales of 5 Å^{-3} for 3D systems, and between 20 and 35 Å^{-3} with scales of 5 Å^{-3} for the 2D systems. Moreover, the `ENCUT` convergence test was performed considering the 1×1×1 structure of MAPbI_3, fixating **k**-density of 25 Å^{-3} and varying f, a multiplicative factor, from 1 to 2.125 in scales of 0.125. This multiplicative factor describes the relation `ENCUT` $= f \times$ `ENMAX`$_{max}$, where `ENMAX`$_{max}$ is the highest `ENMAX` from the atomic species involved.

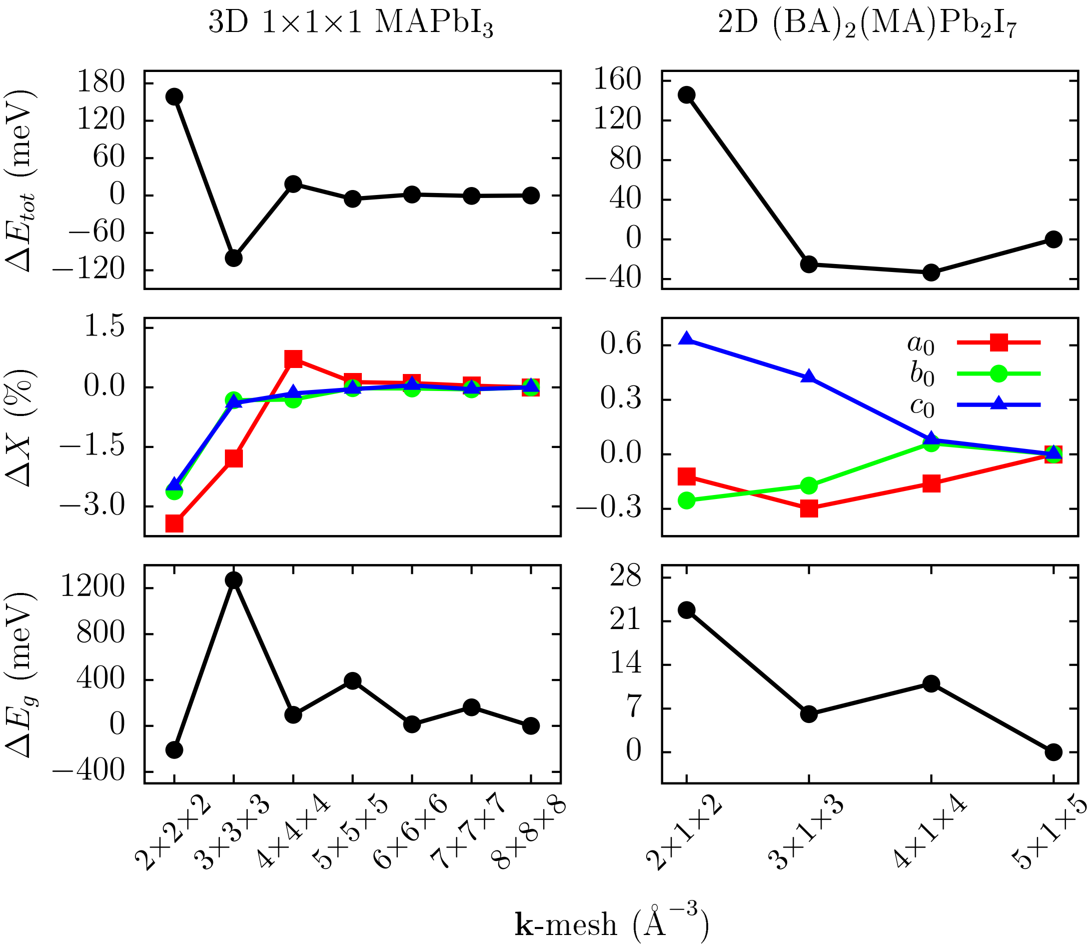

Figure S2 Convergence tests as function of k-mesh for 3D and 2D perovskites. Total energy, lattice parameters and band gap energy relative to the values where the k-mesh equals 8×8×8 **for 3D** 1×1×1 **MAPbI$_3$ and** 5×1×5 **for 2D (BA)$_2$(MA)Pb$_2$I$_7$ perovskites.**

On the left panels of Figure S2 we study the convergence of 1×1×1 MAPbI$_3$ as a function of **k**-mesh by observing the total energy, lattice parameters and the energy gap calculated on Γ point, relative to the values of the referred properties with a 8×8×8 grid. Both total energy and lattice parameters calculations show that the convergence is already observed with a 5×5×5 mesh, while the bottom left panel on Figure S2 shows a band gap deviation of approximately 0.40 eV. The right panels of Figure S2 refer to the 2D perovskite, where the range of values is smaller than that of MAPbI$_3$. A 3×1×3 Å^{-3} mesh presents variation not larger than 30 meV of total energy, 0.50 % on the lattice parameters and

10 meV on the Γ calculated band gap, whereas for $4\times1\times4$ Å^{-3} these values are respectively smaller than 40 meV, 0.20 % and 12 meV.

4.2 Cutoff Energy Convergence Test

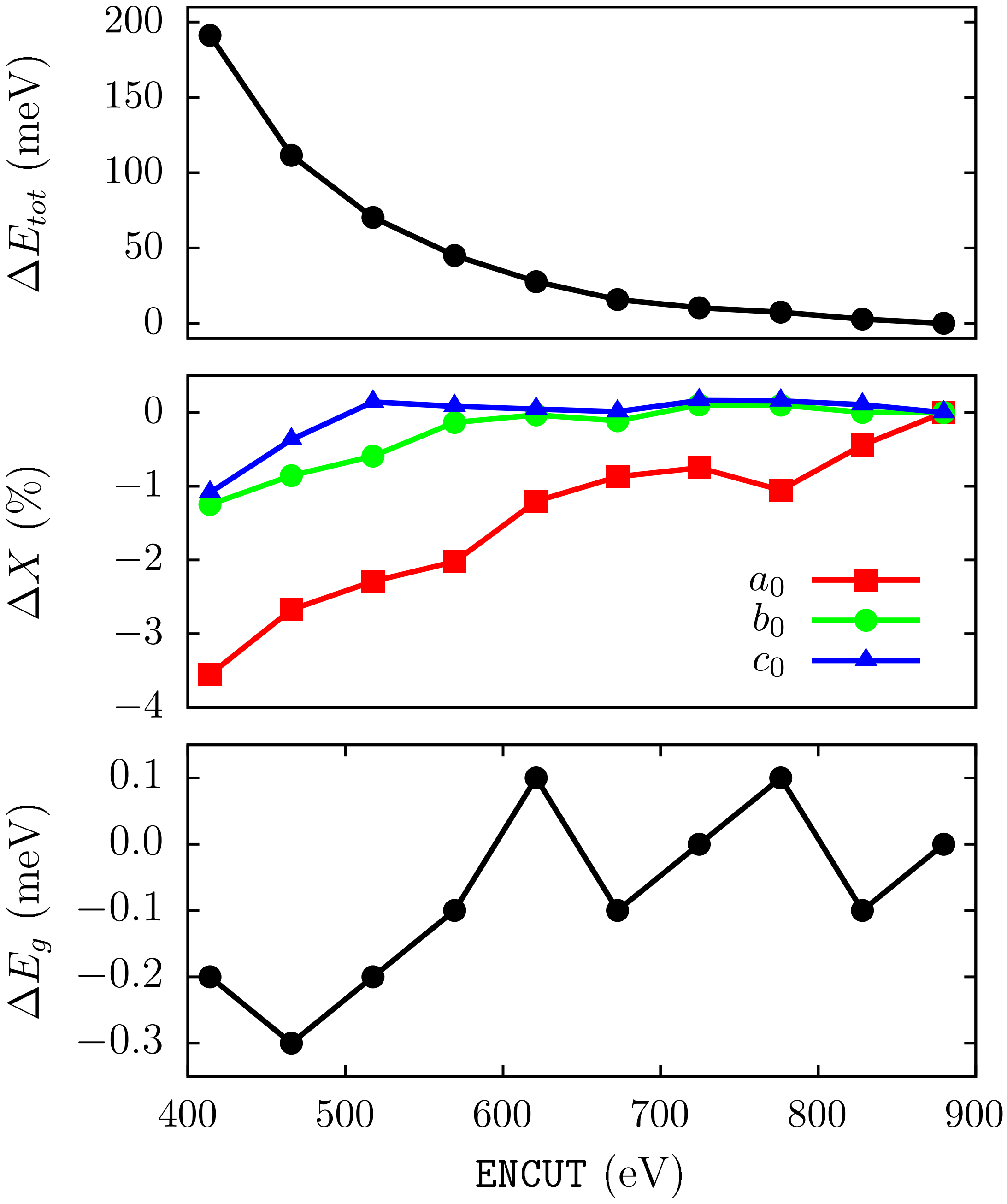

Figure S3 Convergence tests as a function of `ENCUT` **for 3D** $1{\times}1{\times}1$ **MAPbI$_3$ perovskite. Total energy, lattice parameters and band gap energy relative to the values obtained for** `ENCUT` $=$ $2.125 \times$ `ENMAX`$_{max}$.

On Figure S3 we present `ENCUT` convergence tests for the 3D 1×1×1 $MAPbI_3$ while fixing **k**-mesh equals to 5×5×5 $Å^{-3}$. The top panel shows the energy difference related to the total energy for $\texttt{ENCUT} = 2.125 \times \texttt{ENMAX}_{max}$. Considering `ENCUT` higher than 550 eV, the total energy difference is smaller than 50 meV, whereas for values higher than 650 eV, this difference becomes smaller than 20 meV. Furthermore, on the middle panel of Figure S3, we achieve a lattice parameter deviation smaller than 1.5 % when `ENCUT` surpasses 620 eV.

Finally, the bottom panel of Figure S3 has the variation on the energy gap calculated on Γ, but as `ENCUT` is greater than 550 eV this variation is always inside the range of ±1 meV. Both higher values of **k**-mesh and `ENCUT` lead to expensive calculations with greater memory requirements and duration, which is why we selected a **k**-density of 30 $Å^{-3}$ (**k**-meshes of 5×5×5 $Å^{-3}$, 2×2×2 $Å^{-3}$ and 3×1×3 $Å^{-3}$ for 3D 1×1×1, 3D 2×2×2 and 2D structures) while also fixating $\texttt{ENCUT} = 1.50 \times \texttt{ENMAX}_{max}$, 631 eV, to obtain optimized geometries.

4.3 Supercell Approach for the 2D Perovskite

Table S3 Structural parameters for the 2D $(BA)_2(MA)Pb_2I_7$ perovskites considering the unit cell and a $\sqrt{2}\times1\times\sqrt{2}$ supercell: Equilibrium lattice constants (a_0, b_0, c_0), equilibrium volumes of the unit cells (V_0), average octahedral volume ($V_{av}^{oct.}$), average effective coordination number for the B species (ECN_{av}^{B}), and average angles inside (XBX_{av}) and between (BXB_{av}) octahedra. On the last column, we also include the total energy per formula unit (f.u.) (E_{tot})

Struct.	a_0 (Å)	b_0 (Å)	c_0 (Å)	V_0 ($Å^3$)	$V_{av}^{oct.}$ ($Å^3$)	ECN_{av}^{B} (NNN)	XBX_{av} (°)	BXB_{av} (°)	E_{tot} (eV)
unit cell	8.81	42.16	8.64	3205.92	43.38	5.84	176.10	156.65	−246.616 214
supercell	12.48	42.14	12.23	6431.63	43.57	5.84	176.01	156.43	−246.589 706

Table S3 shows the structural parameters for both 2D $(BA)_2(MA)Pb_2I_7$ perovskite structure approximations. The lattice parameters a_0 and c_0 describe the plane where octahedral layers are present, and for them we observe a maximum of 0.17 % difference when comparing the a_0^{super} and c_0^{super} to $a_0^{unit} \times \sqrt{2}$ and $c_0^{unit} \times \sqrt{2}$. On the vertical parameter, however, there is a shrinkage of 0.05 %, which then leads to a 0.31 % increased simulation cell. The average local parameters in $V_{av}^{oct.}$, XBX_{av} and BXB_{av} also show very small deviations, with 0.44 %, −0.05 % and −0.14 %, respectively. Finally, the total energy per formula unit shows that the supercell energy is greater than the one obtained for the unit cell by only 0.01 %. Considering that no deviation surpasses even 0.50 %, the structural parameters obtained by the simple unit cell approach seem to give a fair approximation.

With this simulation, we are also able to compare two supercell approaches: the 2D and the 3D 2×2×2 PbI-based perovskites. The in-plane lattice parameters (12.55 Å and 12.47 Å) and the average octahedra volume (43.42 Å^3) for the 3D $MAPbI_3$ 2×2×2 unit cell depict an optimization of the $PbI_6{}^{4-}$ octahedra, with the in-plane lattice parameters compressing and, to achieve a larger octahedra, the vertical one expanding. However, the relative variations for both cases do not surpass 2 %, meaning that these octahedral layers for the 2D supercell are equivalent to what is observed in the 3D 2×2×2 supercell.

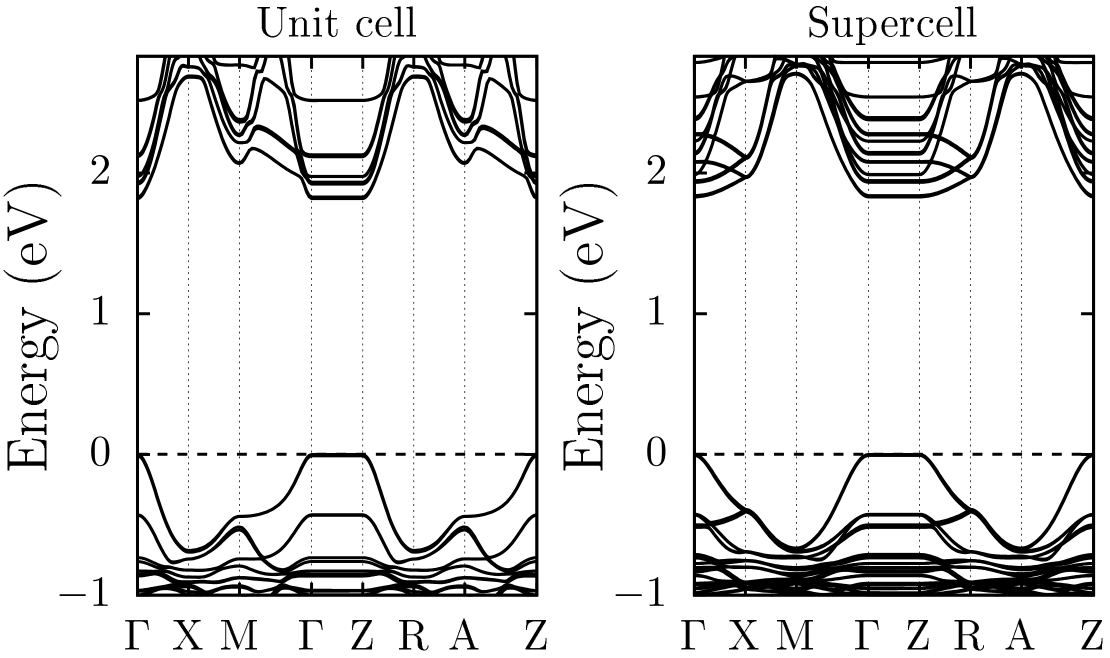

Figure S4 Electronic band structures calculated near the band gap region with the PBE+D3 approximation for the 2D $(BA)_2(MA)Pb_2I_7$ perovskites with an unit cell and a $\sqrt{2}\times1\times\sqrt{2}$ supercell approach. The zero energy is located at the valence band maximum.

To compare optoelectronic properties for unit cell and supercell simulations, we obtained the electronic bands as shown on Figure S4. The different sizes of simulation cells forbid the naive comparison between energy levels for each high-symmetry point, as the reciprocal space is also different. However, we can compare the band gaps observed for these materials, namely 1.70 and 1.83 eV for unit cell and supercell simulations of $(BA)_2(MA)Pb_2I_7$, respectively. Considering that lattice parameter variations are not greater than 0.2 %, the band gap widened by 0.13 eV is an effect of increased degree of freedom in the larger supercell, as discussed in our previous work regarding $CsGeX_3$ perovskites.[8] Thus our 1×1×1 cell of 2D perovskite is a suitable simulation cell.

5 Equilibrium Lattice Parameters: 3D Versus 2D

As discussed on the previous section, we employ a 2×2×2 supercell approach to the 3D perovskites to improve the description of octahedral distortions, where configurations for the other 8 BX combinations (GeCl, GeBr, GeI, SnCl, SnBr, SnI, PbCl and PbBr) were obtained by simple chemical specie exchange and further relaxed using VASP code.

Table S4 and Table S5 show the equilibrium lattice parameters of 3D and 2D perovskites, respectively. Lattice constants, angles between lattice vectors and equilibrium volume of the unit cell, as well as the total energy per formula unit describe the relaxed simulated structures for different BX combinations. Notable trends include the direct correlation of the lattice parameters, unit cell volume and total energy per formula unit with the size of the anion X, as larger atoms increase the crystal size and Cl-based materials have every value lower than Br and I ones for both 3D and 2D structures.

Table S4 Equilibrium PBE+D3 lattice parameters for 3D MABX_3 perovskites with a 2×2×2 supercell: First column presents the BX-sites elements, equilibrium lattice constants (a_0, b_0, c_0), angles between lattice vectors (α, β, γ), equilibrium volume of the unit cell (V_0), and total energy per formula unit (f.u.) (E_{tot}).

BX	a_0 (Å)	b_0 (Å)	c_0 (Å)	α (°)	β (°)	γ (°)	V_0 (Å^3)	E_{tot} (eV)
GeCl	11.02	11.19	11.33	96.18	88.22	91.44	1387.78	−55.221 521
GeBr	11.47	11.70	11.50	92.83	88.19	89.15	1540.49	−53.643 892
GeI	12.13	12.30	12.21	90.85	87.80	88.30	1819.82	−51.968 656
SnCl	11.30	11.50	11.35	87.69	87.51	90.89	1473.69	−55.053 459
SnBr	11.67	11.69	11.78	90.76	86.67	89.66	1603.53	−53.542 877
SnI	12.38	12.53	12.45	89.77	89.92	89.92	1931.53	−51.829 998
PbCl	11.25	11.47	11.36	90.09	89.07	90.87	1465.56	−55.226 693
PbBr	11.77	11.93	11.88	89.75	89.63	90.46	1666.82	−53.668 614
PbI	12.47	12.74	12.55	89.64	89.91	89.59	1994.43	−51.929 460

Table S5 Equilibrium PBE+D3 lattice parameters for 2D (BA)$_2$(MA)B_2X_7 perovskites: First column presents the BX-sites elements, equilibrium lattice constants (a_0, b_0, c_0), angles between lattice vectors (α, β, γ), equilibrium volume of the unit cell (V_0), and total energy per formula unit (f.u.) (E_{tot}).

BX	a_0 (Å)	b_0 (Å)	c_0 (Å)	α (°)	β (°)	γ (°)	V_0 (Å^3)	E_{tot} (eV)
GeCl	7.98	38.98	7.44	86.67	89.84	89.93	2309.73	−254.166 608
GeBr	8.18	39.45	7.71	87.28	89.96	90.33	2487.10	−250.581 142
GeI	8.54	40.72	8.23	86.76	89.78	90.51	2857.44	−246.702 683

Continues on next page

Table S5 – continued from previous page

BX	a_0 (Å)	b_0 (Å)	c_0 (Å)	α (°)	β (°)	γ (°)	V_0 (Å^3)	E_{tot} (eV)
SnCl	8.12	39.51	7.53	89.15	90.14	89.61	2416.87	−253.997 883
SnBr	8.25	40.21	7.98	86.92	89.59	90.21	2643.10	−250.518 646
SnI	8.74	41.78	8.50	88.53	89.29	89.92	3102.48	−246.458 910
PbCl	8.06	39.98	7.64	88.77	90.01	89.98	2458.83	−254.354 105
PbBr	8.30	40.59	8.06	87.05	89.77	89.46	2711.36	−250.789 147
PbI	8.81	42.16	8.64	88.61	88.89	89.67	3205.92	−246.616 214

6 Local Structural Parameters: 3D Versus 2D

Octahedral distortions are present on the studied systems, and in that case, we present a series of histograms for the following properties of 3D and 2D structures: octahedral volumes, V_{oct}, bond lengths between B and X atoms, effective coordination number for the B atom that is located at the center of the octahedra, ECN^B, and bond angles between atoms X–B–X (X atoms on opposite sides of the octahedra) and B–X–B (between octahedra). Average values for ECN^B and bond angles are shown on Figure S5.

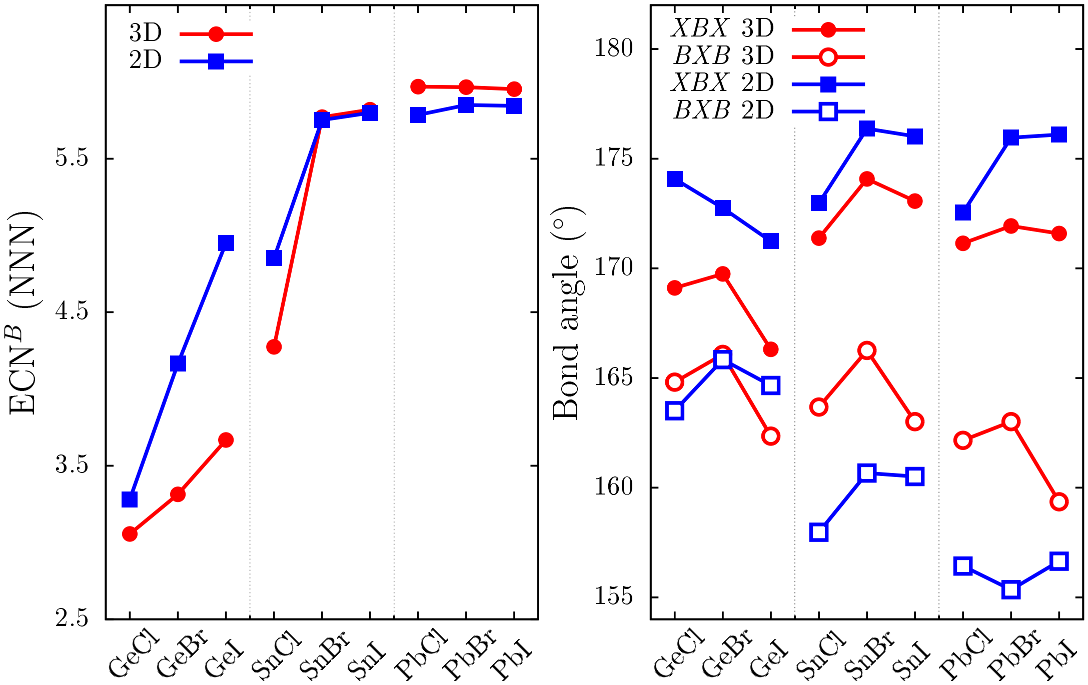

Figure S5 Average effective coordination number for the B-site atom, ECN^B, and average bond angles inside and between octahedra, XBX and BXB, for 3D MABX_3 and 2D (BA)$_2$(MA)B_2X_7 perovskites.

6.1 Octahedral Volumes

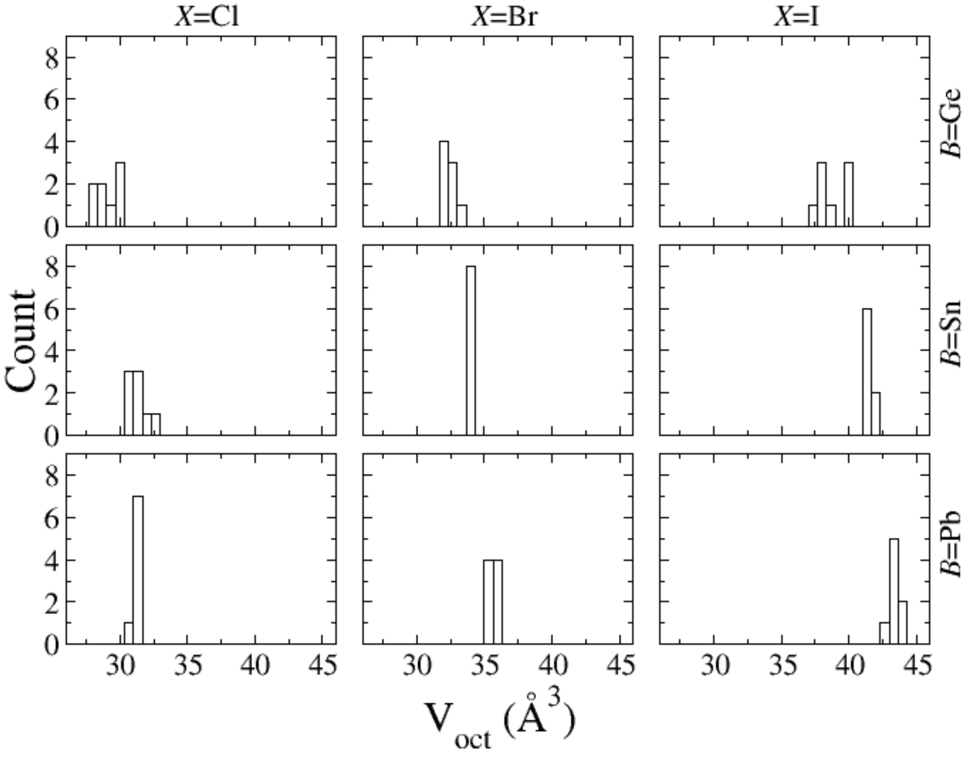

Figure S6 Histograms for BX_6 octahedral volumes of 3D MABX_3 perovskites.

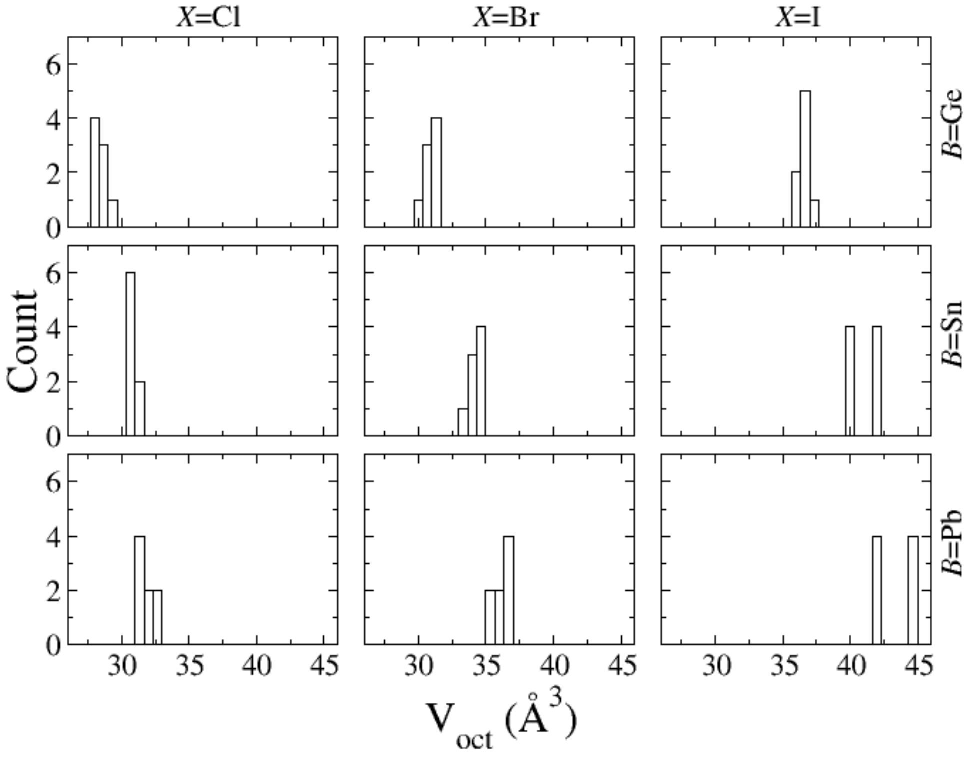

Figure S7 Histograms for BX_6 octahedral volumes of 2D $(BA)_2(MA)B_2X_7$ perovskites.

From both Figures S6 and S7, we note how volumes increase as B and X atoms radii size also increase. Comparing 3D and 2D structures, we also notice that, for the more regular octahedra in Ge-based in 2D perovskites, the 2D octahedral volumes are smaller than their counterparts.

6.2 B–X Bond Length

Between Figure S8 and Figure S9, we note how bond lengths are spread in Ge-based materials and converge to an average value when increasing the B atom size. This is attributed to the higher Jahn–Teller distortions that come from the presence of Ge atoms. Increasing X atoms size mainly increase the average bond lengths, but by comparing 3D and 2D structures, layered perovskites with Ge do not have groups of values, but a large spread of lengths, meaning that although there are still distortions from these octahedra, the ones for 2D systems are reduced.

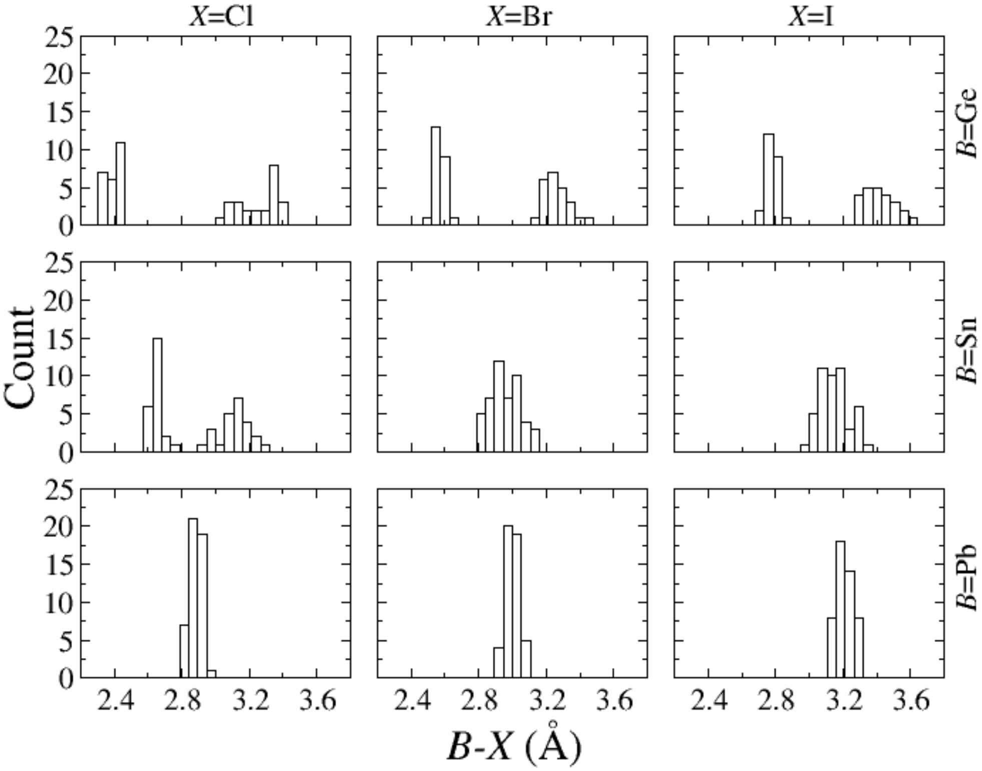

Figure S8 Histograms for the bond lengths B–X for the 3D MABX_3 compounds.

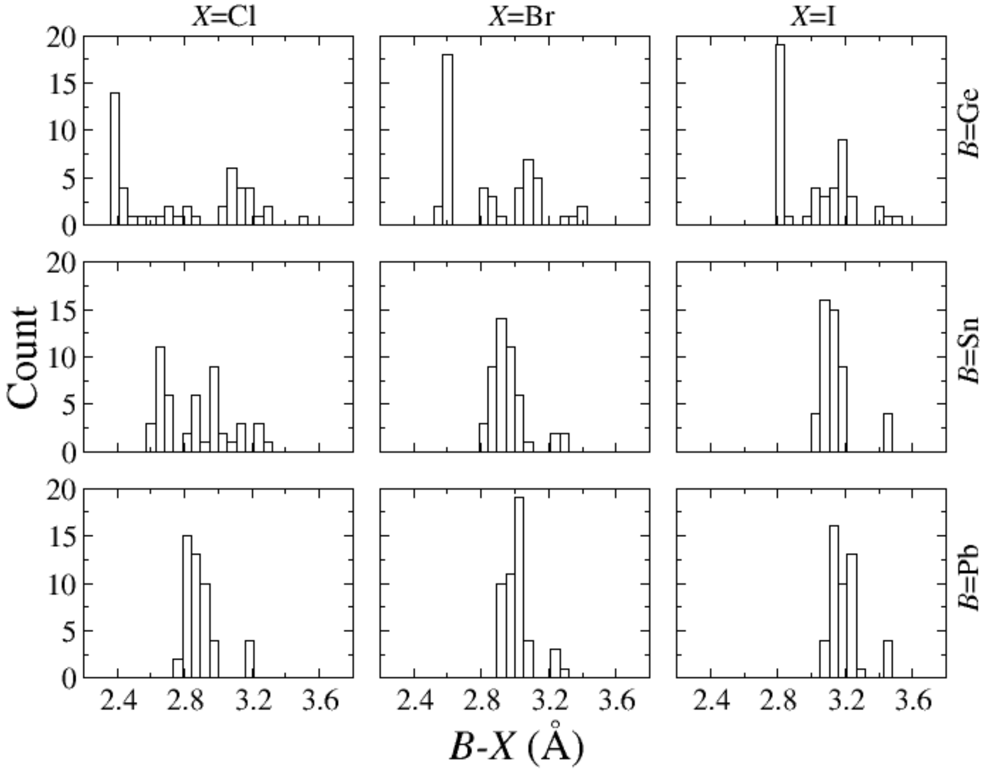

Figure S9 Histograms for the bond lengths B–X for the 2D (BA)$_2$(MA)B_2X_7 compounds.

6.3 Effective Coordination Number of B Sites.

The effective coordination number (ECN) for the B atoms (ECN^B) located in the center of the octahedra was obtained by the Visualization for Electronic and Structural Analysis (VESTA) software[9] based on the effective coordination concept. The ECN parameter is calculated by the following equation,

$$ECN = \sum_i \exp\left[1 - \left(\frac{l_i}{l_{av}}\right)^6\right], \tag{2}$$

where the ECN is obtained as the sum of different bond contributions (l_i). The weighted average bond length (l_{av}) is defined by the following equation,

$$l_{av} = \frac{\sum_i l_i \exp\left[1 - (l_i/l_{min})^6\right]}{\sum_i \exp\left[1 - (l_i/l_{min})^6\right]} \, , \tag{3}$$

where l_{min} is the smallest bond length within the selected polyhedron.

As discussed from the B–X bond lengths, the ECN^B results describe the same behavior from the octahedral distortions. From Figures S10 and S11, the octahedra also tend have ECN^B closer to 6 NNN as B and X atoms radii increase.

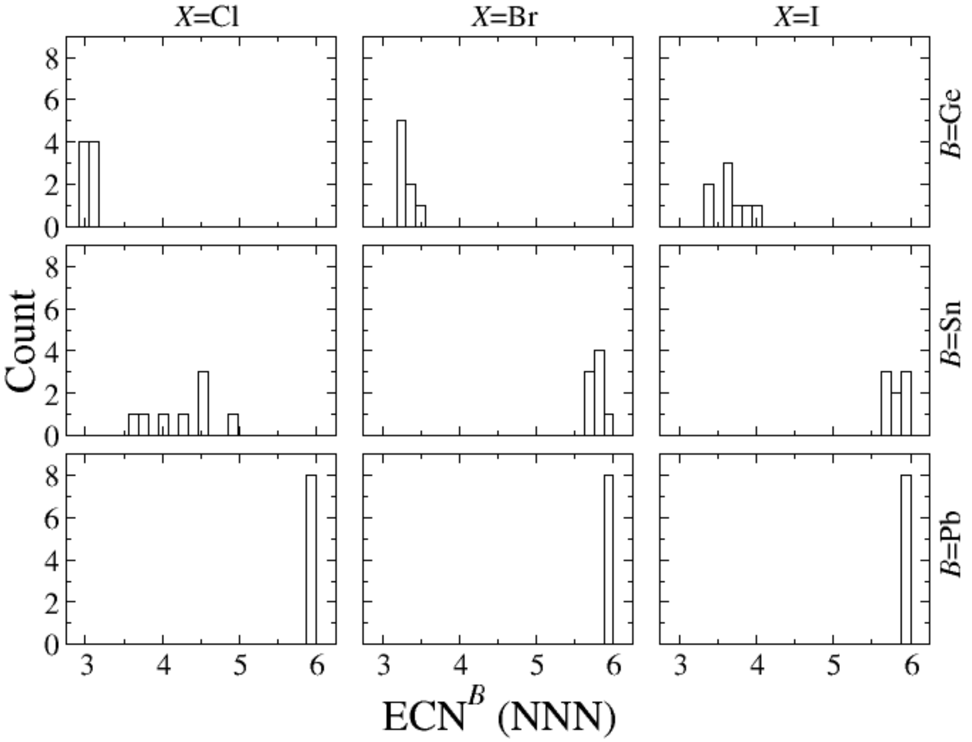

Figure S10 Histograms for BX_6 octahedral effective coordination number for the 3D MABX_3 compounds.

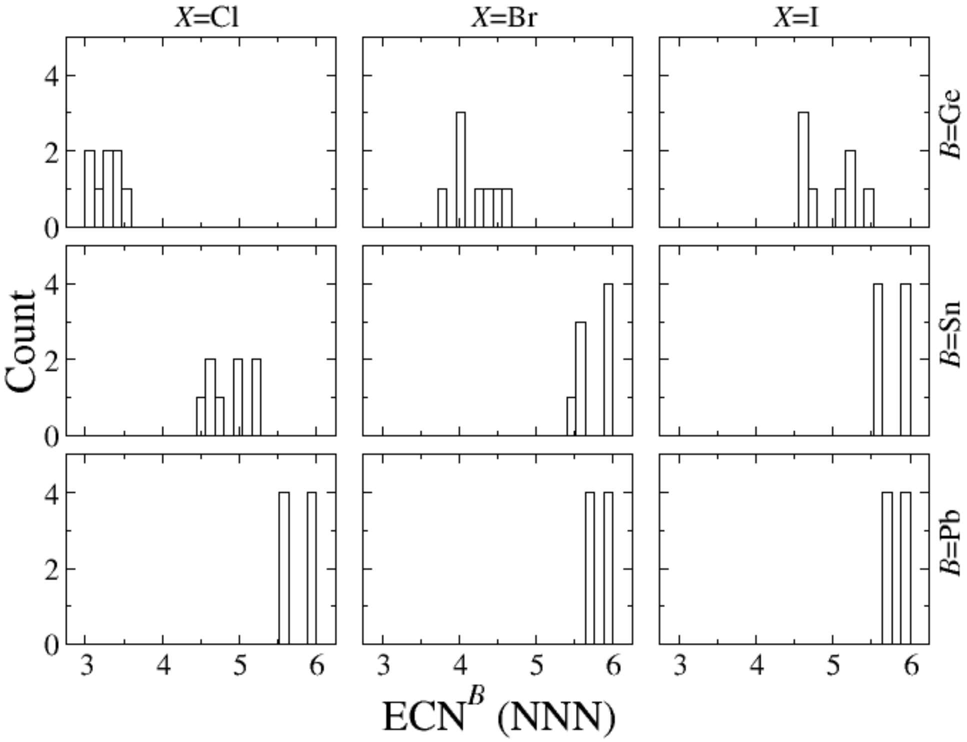

Figure S11 Histograms for BX_6 octahedral effective coordination number for the 2D $(BA)_2(MA)B_2X_7$ compounds.

6.4 XBX Bond Angle

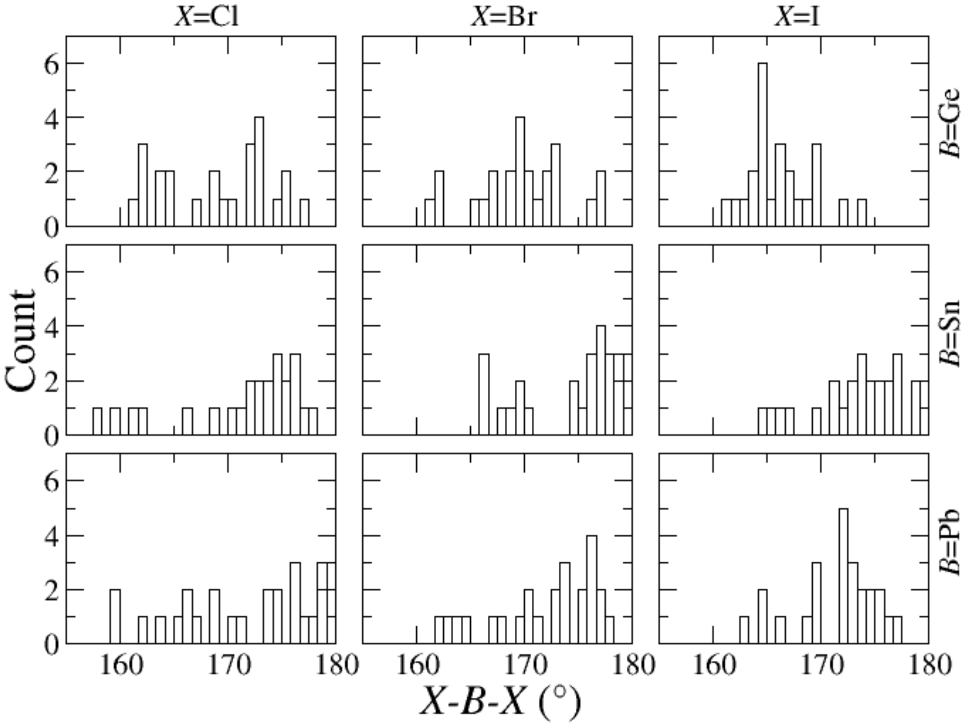

Figure S12 Histograms for the angle between atoms X–B–X, with X on opposite sides of the octahedra, of 3D MABX_3 perovskites.

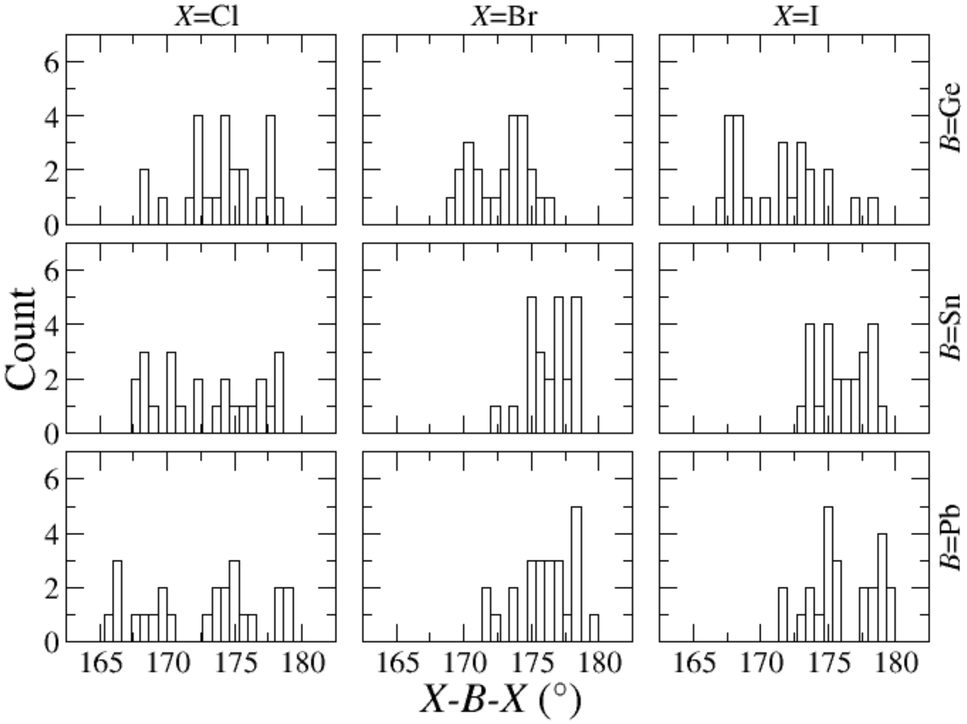

Figure S13 Histograms for the angle between atoms *X*–*B*–*X*, with *X* on opposite sides of the octahedra, of 2D (BA)$_2$(MA)B_2X_7 perovskites.

The X–B–X angles inside octahedra, with X atoms being on opposite sides, are shown on Figure S12 and Figure S13. We note that for 2D perovskites, their values are greater than those of the bulk, which is another measure of the regularity of octahedra following the BA inclusion on bulk metal halide perovskites.

6.5 *BXB* Bond Angle

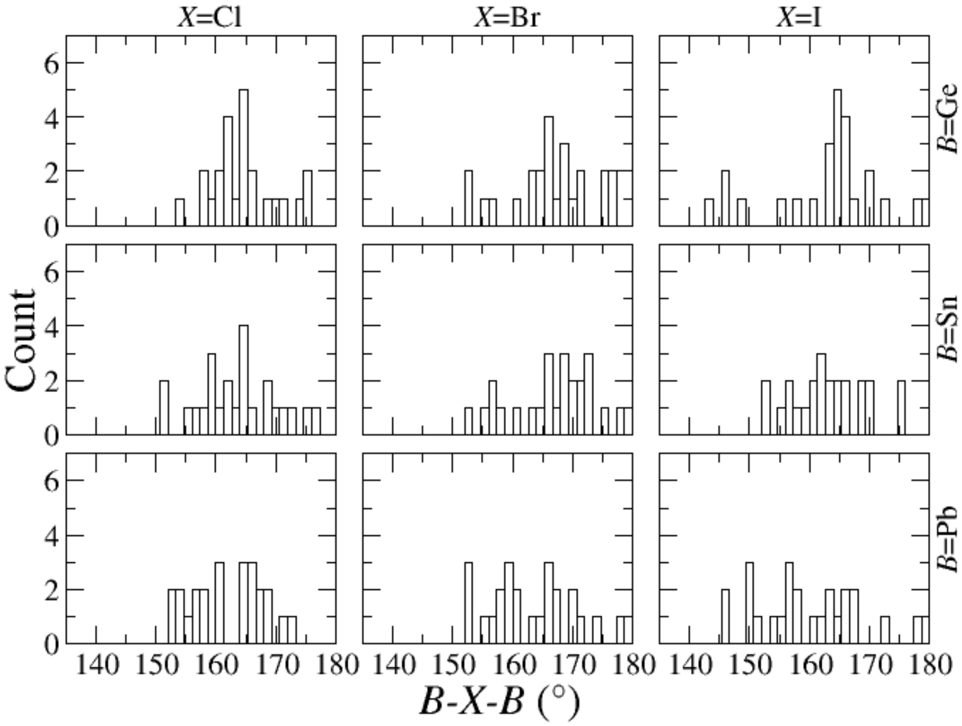

Figure S14 Histograms for the angle between atoms *B*–*X*–*B*, connecting octahedra, of 3D MABX_3 perovskites.

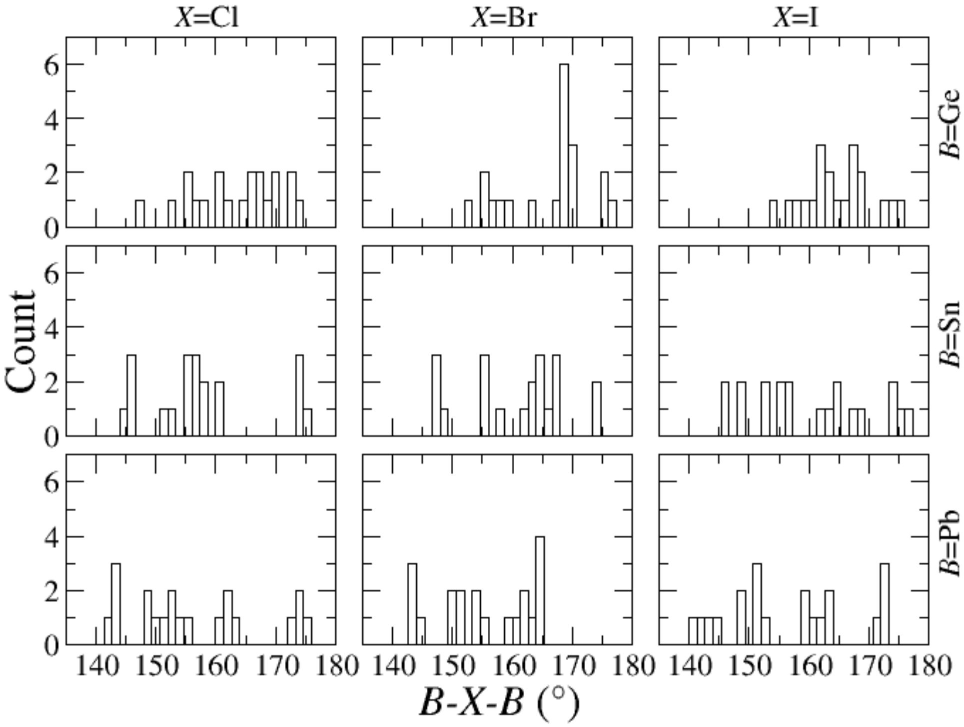

Figure S15 Histograms for the angle between atoms *B*–*X*–*B***, connecting octahedra, of 2D (BA)$_2$(MA)B_2X_7 perovskites.**

From Figure S14 and Figure S15, we note the angles between octahedra. Bulk structures show Sn- and Pb-based perovskites with more values at higher angles, which would mean that there are greater distortions between octahedra in the 2D perovskites. On the other hand, GeI-based materials show an opposite behavior, with smaller values near 145° for 3D perovskites, which pull down the average value and makes the average 2D value higher than for 3D.

7 Energetic Properties: 3D Versus 2D

The cohesive energy is defined in this work as,

$$E_{coh} = E_{tot} - \sum_{i=1}^{N} E_i \; , \tag{4}$$

where E_{tot} is the total energy of the perovskite, N is the total number of atoms and E_i is the total energy of each isolated atom present in the material. To perform a cohesive energy decomposition, we separate the N atomic species in N^{BA}, N^{MA} and $N^{oct.}$ as the number of atomic species present in the organic spacer BA (for the 2D perovskites), in the MA organic molecule and in the inorganic octahedra. For each of those terms, j, we write their cohesive energy, E^{j}_{coh}, as:

$$E^{j}_{coh} = E^{j}_{tot} - \sum_{i=1}^{N^{j}} E_i \; . \tag{5}$$

The total energies for the constituents, E^{j}_{tot}, are obtained by selecting the atoms present in j and removing those not present while maintaining the structure and the N^{j} atoms frozen. We also define an interaction energy as the difference of the total energy of the material and its constituents, or:

$$E^{int.}_{coh} = E_{tot} - E^{\mathrm{BA}}_{tot} - E^{\mathrm{MA}}_{tot} - E^{oct.}_{tot} \; . \tag{6}$$

The equation above holds true for the 2D perovskite, while for the 3D ones, as there are no spacer molecules, we disregard the term E^{BA}_{tot}.

By adding equations 5 and 6, we obtain

$$\begin{aligned} E^{\mathrm{BA}}_{coh} + E^{\mathrm{MA}}_{coh} + E^{oct.}_{coh} + E^{int.}_{coh} &= E_{tot} - \sum_{i=1}^{N^{\mathrm{BA}}} E_i - \sum_{i=1}^{N^{\mathrm{MA}}} E_i - \sum_{i=1}^{N^{oct.}} E_i \\ &= E_{tot} - \sum_{i=1}^{N} E_i \; . \end{aligned} \tag{7}$$

And, by comparing equations 4 and 7, we obtain another expression for the cohesive energy as a function as the cohesive energy of its constituents, given by:

$$E_{coh} = E_{coh}^{\mathrm{BA}} + E_{coh}^{\mathrm{MA}} + E_{coh}^{oct.} + E_{coh}^{int.} \,. \tag{8}$$

Table S6 Decomposition of the cohesive energies, in eV, in its contributions (E_{coh}^{BA}, E_{coh}^{MA}, $E_{coh}^{oct.}$, $E_{coh}^{int.}$) for the 3D MABX_3 and 2D (BA)$_2$(MA)B_2X_7 perovskites. E_{coh}^{BA}, E_{coh}^{MA}, $E_{coh}^{oct.}$, and $E_{coh}^{int.}$ indicate the organic spacer, organic MA molecule, inorganic frame, and the interaction energy between the molecules and inorganic framework contributions, respectively. First and last columns indicate the BX species and the cohesive energy per atom (E_{coh}^{atom}).

BX	Struct.	E_{coh}	E_{coh}^{BA}	E_{coh}^{MA}	$E_{coh}^{oct.}$	$E_{coh}^{int.}$	E_{coh}^{atom}
GeCl	3D	−336.96	–	−212.10	−82.60	−42.26	−3.51
	2D	−778.55	−522.89	−105.53	−83.22	−66.90	−3.82
GeBr	3D	−326.78	–	−211.57	−75.05	−40.16	−3.40
	2D	−767.04	−522.81	−105.41	−76.53	−62.29	−3.76
GeI	3D	−314.68	–	−211.07	−67.21	−36.40	−3.28
	2D	−753.05	−522.40	−105.17	−68.64	−56.84	−3.69
SnCl	3D	−336.50	–	−211.88	−84.08	−40.55	−3.51
	2D	−778.76	−523.00	−105.48	−86.07	−64.21	−3.82
SnBr	3D	−326.85	–	−211.18	−77.13	−38.54	−3.40
	2D	−767.68	−523.04	−105.31	−79.14	−60.19	−3.76
SnI	3D	−314.45	–	−210.74	−68.18	−35.54	−3.28
	2D	−752.96	−522.05	−105.03	−70.41	−55.47	−3.69
PbCl	3D	−338.35	–	−211.74	−81.98	−44.63	−3.52
	2D	−780.64	−523.29	−105.48	−82.22	−69.66	−3.83
PbBr	3D	−328.32	–	−211.29	−75.04	−41.99	−3.42
	2D	−769.22	−523.09	−105.28	−75.79	−65.06	−3.77

Continues on next page

Table S6 – continued from previous page

BX	Struct.	E_{coh}	E_{coh}^{BA}	E_{coh}^{MA}	$E_{coh}^{oct.}$	$E_{coh}^{int.}$	E_{coh}^{atom}
PbI	3D	-315.71	–	-210.63	-66.86	-38.22	-3.29
	2D	-754.05	-522.11	-105.04	-67.97	-58.93	-3.70

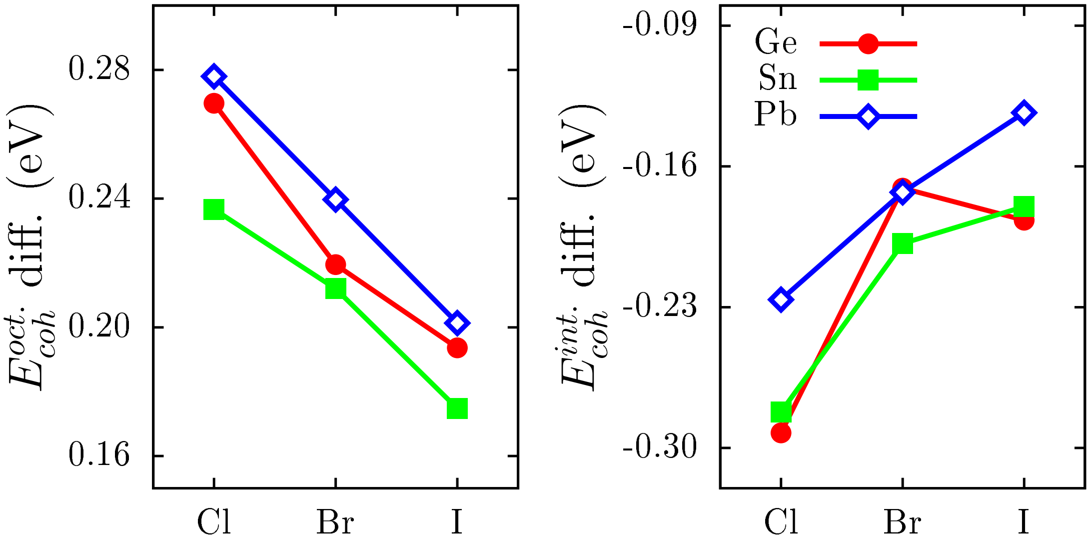

Figure S16 **$E_{coh}^{oct.}$ and $E_{coh}^{int.}$ differences, in eV, between 2D (BA)$_2$(MA)B_2X_7 and 3D MABX_3 perovskites.**

7.1 Formation Enthalpy Calculation

Formation enthalpy (ΔH_f) gives us the energetic cost to obtain any model system, which references its individual constituents.

For our perovskite models, we can define the formation enthalpy as follows:

$$\Delta H_f^{2D} = \frac{1}{N^{\mathrm{X}}} \left\{ E_{tot}^{(\mathrm{BA})_8(\mathrm{MA})_4(B_2X_7)_4} - \left(8E_{tot}^{\mathrm{BX_2}} + 8E_{tot}^{\mathrm{BAX}} + 4E^{\mathrm{MAX}} \right) \right\} \tag{9}$$

for 2D models, and

$$\Delta H_f^{3D} = \frac{1}{N^X}\left\{E_{tot}^{\mathrm{MA}_8(BX_3)_8} - \left(8E_{tot}^{\mathrm{BX}_2} + 8E_{tot}^{\mathrm{MAX}}\right)\right\} \tag{10}$$

for 3D one (M= Ge, Sn, Pb, and X= Cl, Br, I). $E_{tot}^{\mathrm{BX}_2}$, E_{tot}^{BAX}, and E_{tot}^{MAX} are the total energy of the BX_2, MAX, and BAX respectively. N^X is the number of halides in the perovskite model.

Now we want to compare the 3D formation enthalpy with the 2D one. For this, we further analyze each term of Equations 9 and 10, considering the constituents in the gas phase (g label). For the 3D model, we write the total energies in the following way:

$$E_{tot}^{\mathrm{MA}_8(BX_3)_8} = E_{coh}^{\mathrm{MA}_8(BX_3)_8} + \sum_i^{N^C} E_i^C + \sum_i^{N^\mathrm{N}} E_i^\mathrm{N} + \sum_i^{N^\mathrm{H}} E_i^\mathrm{H} + \sum_i^{N^B} E_i^B + \sum_i^{N^X} E_i^X\ ;$$

$$E_{tot}^{BX_2(g)} = E_{coh}^{BX_2} + E_i^B + \sum_i^{2} E_i^X\ ;$$

$$E_{tot}^{\mathrm{MA}X(g)} = E_{coh}^{\mathrm{MA}X} + E_i^C + E_i^\mathrm{N} + \sum_i^{6} E_i^\mathrm{H} + E_i^X\ .$$

Put it in the Equation 10, we have

$$\Delta H_f^{3D} = \frac{1}{N^X}\left(E_{coh}^{\mathrm{MA}_8(BX_3)_8} + \sum_i^{8} E_i^C + \sum_i^{8} E_i^\mathrm{N} + \sum_i^{48} E_i^\mathrm{H} + \sum_i^{8} E_i^B + \sum_i^{N^X} E_i^X\right) + \\ -\frac{8}{N^X}\left(E_{coh}^{BX_2(g)} + \sum_i^{1} E_i^B + \sum_i^{2} E_i^X\right) - \frac{8}{N^X}\left(E_{coh}^{\mathrm{MA}X(g)} + E_i^C + E_i^\mathrm{N} + \sum_i^{6} E_i^\mathrm{H} + E_i^X\right)\ , \tag{11}$$

what give us

$$\Delta H_f^{3D} = \frac{1}{N^X}\left\{E_{coh}^{\mathrm{MA}_8(BX_3)_8} - 8\left(E_{coh}^{BX_2(g)} + E_{coh}^{\mathrm{MA}X(g)}\right)\right\}\ . \tag{12}$$

The same result is valid for a solid phase (s label) reference. Since we have the cohesive energy per formula unit of BX_2 in the solid phase, we can write:

$$\Delta H_f^{3D} = \frac{1}{N^X}\left\{E_{coh}^{\mathrm{MA}_8(BX_3)_8} - 8\left(E_{coh}^{BX_2(s)} + E_{coh}^{\mathrm{MA}X(g)}\right)\right\}\ . \tag{13}$$

The above analyses can be performed on the 2D model. Since we know the cohesive energy of the BAX molecule ($E_{coh}^{\mathrm{BA}X}$) we have

$$\Delta H_f^{2D} = \frac{1}{N^X} \left\{ E_{coh}^{(\mathrm{BA})_8(\mathrm{MA})_4(B_2X_7)_4} - \left(8E_{coh}^{BX_2} + 8E_{coh}^{BAX} + 4E_{coh}^{\mathrm{MA}X} \right) \right\} . \tag{14}$$

Finally, we have the expression for the formation enthalpy as a function of cohesive energy, allowing further quantification of the structural stability of our models. Once in the decomposition process, the broken bonds of B-X lead to the formation of individual constituents. We can write the enthalpy of formation per number of halides (N^X) in order to correctly compare the formation enthalpy energy of the 3D model with that of the 2D model

7.1.1 Total Energies Calculation of Constituents

To obtain the total energies of constituents, we perform the following steps:

Gas phase

1. First, we place the molecule in an orthorhombic box, where the lattice parameters were chosen in a way to keep a minimal distance of 15 Å between the molecule and its image, taking into account the molecule size in each direction.
2. Including a cutoff energy of 473.514 750 eV, `ISIF` $= 0$, **k**-grid of $1\times1\times1$, and `SPIN` $= 2$, and using selective dynamics, we optimize the atomic positions of the X site only.
3. After obtaining the optimized X site in relation to the MA, we remove the selective dynamics and optimize the atomic positions of the entire molecule using the same cutoff as in the previous steps (the same one used for the total energy calculation of 2D and 3D perovskite).
4. The BX_2 models were optimized without any steps of selective dynamics.

Solid phase

1. First, we select the structure in the Materials Project and perform a stress tensor

calculation, including an `ENCUT` $= 1.5$`ENMAX`$_{\text{max}}$, `ISIF` $= 3$, $\mathbf{k}$-density of $30R_k$. Here, we use a step-by-step procedure, including `NSW` $= 5, 10, 20, 40, ...$, until a constant regime is reached for the total volume and lattice parameters.

2. After obtaining the optimized lattice parameters, we perform an optimization of atomic positions only to minimize the forces on each atom. For this, we use `ISIF` $= 0$ and a cutoff energy of 473.514 750 eV .

Table S7 PBE+D3 structural parameters, including maximum and minimum values for solid-phase SnI_2 and $PbCl_2$ models. $d^{AX}_{\mathrm{H}-X}$ is $\mathrm{H} - X$ bonding length at AX constituents, $d^{AX}_{\mathrm{N-H}}$ is $\mathrm{N - H}$ bonding length at AX molecule, and $d^{BX_2}_{B-X}$ is the $B - X$ bonding length at BA component.

AX	$d^{AX(\mathrm{g})}_{\mathrm{H}-X}$ (Å)	$d^{AX(\mathrm{g})}_{\mathrm{N-H}}$ (Å)	BX_2	$d^{BX_2(\mathrm{s})}_{M-X}$ (Å)	$d^{BX_2(\mathrm{g})}_{M-X}$ (Å)
MACl	1.46	1.42	$GeCl_2$	2.67	2.21
MABr	1.75	1.24	$GeBr_2$	2.80	2.36
MAI	2.04	1.18	GeI_2	3.02	2.58
BACl	1.47	1.41	$SnCl_2$	3.05	2.39
BABr	1.77	1.23	$SnBr_2$	3.01	2.54
BAI	2.05	1.17	SnI_2	3.16/3.25	2.75
			$PbCl_2$	2.83/2.87	2.49
			$PbBr_2$	3.05	2.63
			PbI_2	3.24	2.83

Table S8 Formatiom enthalpy of 3D and 2D model, including solid phase ($\Delta H_f^{(s)}$) and gas pahs phse ($\Delta H_f^{(g)}$ reference. PBE+D3 total energy of constituents. $E_{tot}^{AX(\mathrm{g})}$ is total energy of AX in gas phase, $E_{tot}^{BX_2(\mathrm{s})}$ is total energy of BX_2 in solid phase, and $E_{tot}^{BX_2(\mathrm{g})}$ is total energy of BX_2 in gas phase.

BX	Struct.	$\Delta H_f^{(s)}/\Delta H_f^{(g)}$	BX_2	$E_{tot}^{BX_2(\mathrm{s})}$	$E_{tot}^{BX_2(\mathrm{g})}$	AX	$E_{tot}^{AX(\mathrm{g})}$
		(eV/N^X)		(eV/f.u.)	(eV)		(eV)
GeCl	3D	$-0.96/-0.70$	$GeCl_2$	$-10.831\,371$	$-10.038\,784$	MACl	$-42.299\,488$
	2D	$-1.12/-0.90$	–	–	–	BACl	$-91.958\,133$

Continues on next page

Table S8 – continued from previous page

BX	Struct.	$\Delta H_f^{(s)}(\Delta H_f^{(g)})$ (eV/N^X)	BX_2	$E_{tot}^{BX_2(\mathrm{s})}$ (eV/f.u.)	$E_{tot}^{BX_2(\mathrm{g})}$ (eV)	AX	$E_{tot}^{AX(\mathrm{g})}$
GeBr	3D	−1.01/−0.68	$GeBr_2$	−9.909 206	−8.923 221	MABr	−41.686 236
	2D	−1.19/−0.91	–	–	–	BABr	−91.351 644
GeI	3D	−1.05/−0.57	GeI_2	−9.184 401	−7.743 727	MAI	−41.082 379
	2D	−1.23/−0.82	–	–	–	BAI	−90.752 562
SnCl	3D	−1.01/−0.59	$SnCl_2$	−10.978 674	−9.709 201	–	–
	2D	−1.19/−0.83	–	–	–	–	–
SnBr	3D	−1.07/−0.64	$SnBr_2$	−9.940 723	−8.659 687	–	–
	2D	−1.26/−0.89	–	–	–	–	–
SnI	3D	−1.07/−0.58	SnI_2	−9.019 955	−7.528 903	–	–
	2D	−1.26/−0.83	–	–	–	–	–
PbCl	3D	−1.17/−0.61	$PbCl_2$	−11.090 975	−9.411 815	–	–
	2D	−1.33/−0.85	–	–	–	–	–
PbBr	3D	−1.18/−0.62	$PbBr_2$	−10.137 152	−8.441 204	–	–
	2D	−1.36/−0.88	–	–	–	–	–
PbI	3D	−1.15/−0.54	PbI_2	−9.224 477	−7.385 337	–	–
	2D	−1.32/−0.80					

8 Effective Bader Charge: 3D Versus 2D

Table S9 Effective Bader charge, Q_{Bader}, for the constituents of the 3D MABX_3 and 2D (BA)$_2$(MA)B_2X_7 perovskites. First column presents the BX-sites elements.

BX	Struct.	$Q^{\text{BA}}_{\text{Bader}}$	$Q^{\text{MA}}_{\text{Bader}}$	Q^{B}_{Bader}	Q^{X}_{Bader}
GeCl	3D	–	6.46	8.81	−15.28
	2D	6.40	3.14	8.88	−18.42
GeBr	3D	–	6.24	7.46	−13.70
	2D	6.15	3.00	7.53	−16.69
GeI	3D	–	5.89	5.56	−11.45
	2D	5.81	2.83	5.59	−14.23
SnCl	3D	–	6.42	10.12	−16.54
	2D	6.37	3.12	10.11	−19.60
SnBr	3D	–	6.24	9.01	−15.25
	2D	6.11	3.00	8.97	−18.08
SnI	3D	–	5.93	7.41	−13.34
	2D	5.90	2.85	7.23	−15.98
PbCl	3D	–	6.39	10.22	−16.61
	2D	6.33	3.10	10.12	−19.54
PbBr	3D	–	6.20	9.05	−15.25
	2D	6.05	2.98	8.99	−18.02
PbI	3D	–	5.92	7.59	−13.51
	2D	5.86	2.85	7.40	−16.11

The Bader charges presented on Table S9 are the total charges for each part of the perovskites as obtained from the code obtained by Henkelman et al.[10] E.g. for both organic molecules, the result is the sum of the charges for C, N and H species located on each molecule. Values for Q^{B}_{Bader} are comparable between 2D and 3D structures, as we note that only for Ge-based perovskites the charge transference is higher for 2D systems. It is also possible to compare $Q_{\text{Bader}}^{\text{MA}}$, as there are twice MA molecules on 3D systems, resulting in greater Bader charge for 3D systems.

9 Density of States: 3D Versus 2D

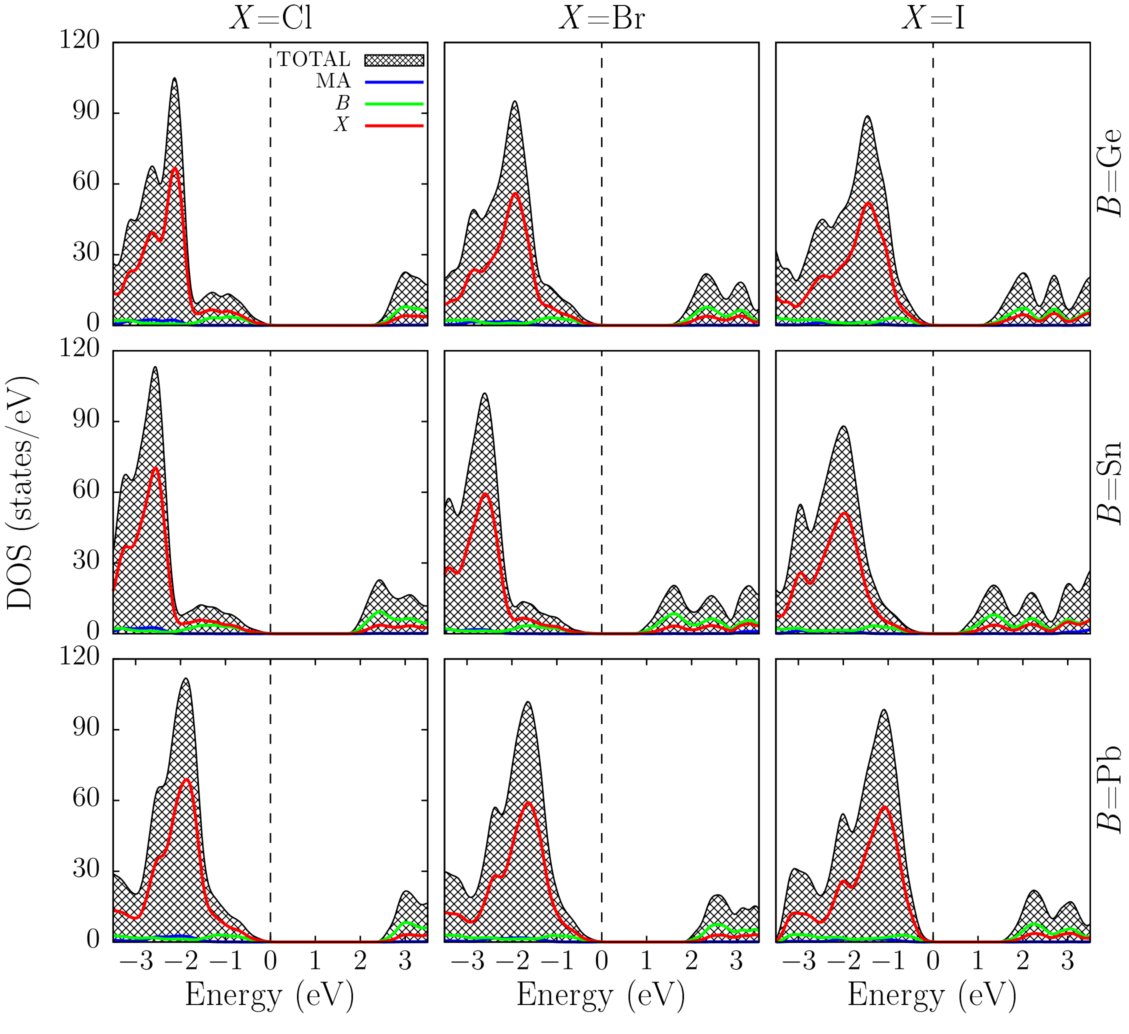

Figure S17 Local density of states obtained by the PBE+D3 calculations for the 3D MABX_3 perovskites. The vertical dashed lines indicate the valence band maximum.

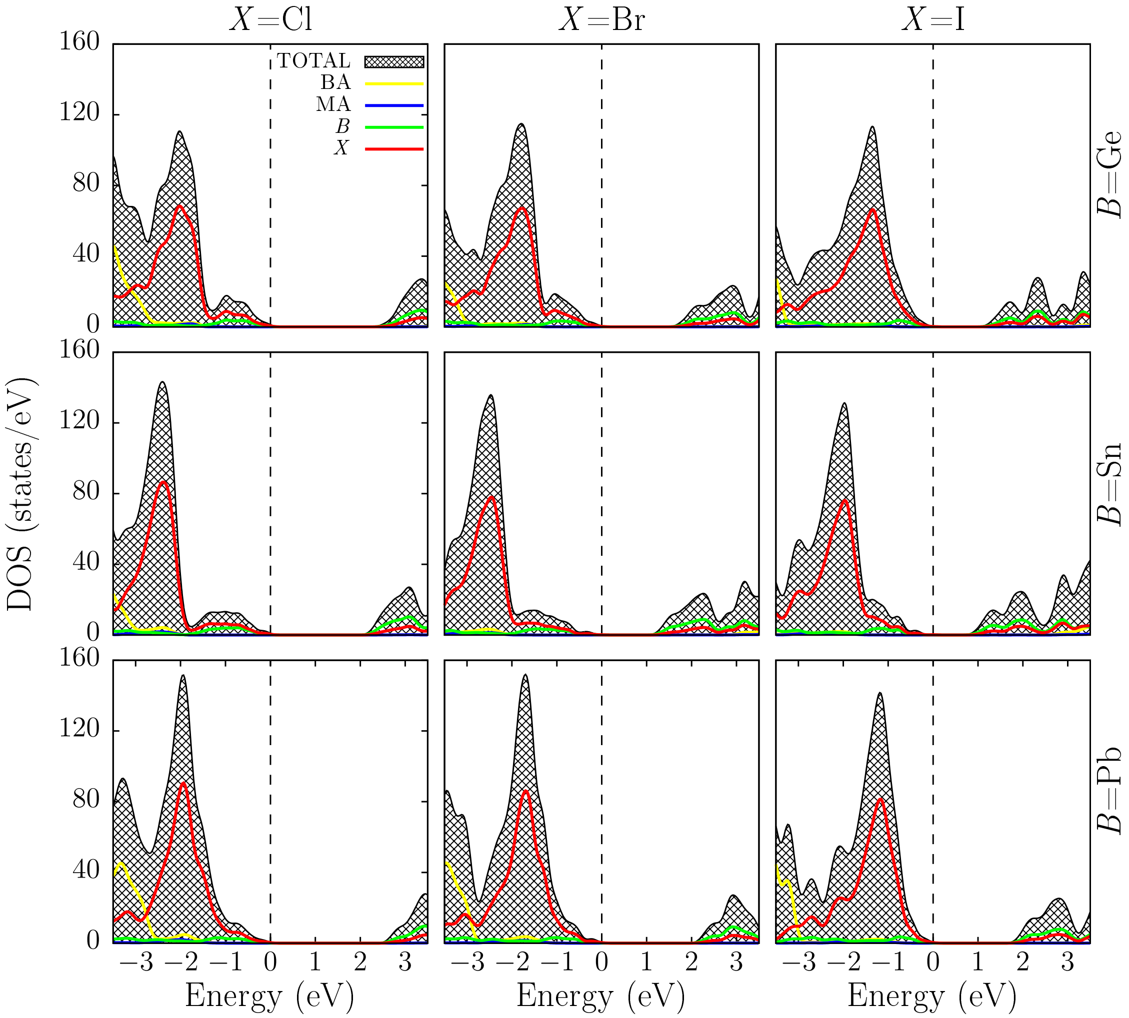

Figure S18 Local density of states obtained by the PBE+D3 calculations for the 2D $(BA)_2(MA)B_2X_7$ perovskites. The vertical dashed lines indicate the valence band maximum.

10 Electronic Band Structures: 3D Versus 2D

Since the 3D perovskites $MABX_3$ presents a cubic lattice, however, with local distortions, the high-symmetry points from a cubic cell presented on Figure S19 are used in the electronic bands calculation. 2D perovskites with formula $(BA)_2(MA)B_2X_7$, on the other hand, present a tetragonal structure, where the high-symmetry points from a generic unit cell used in the electronic bands calculation are presented on Figure S20.

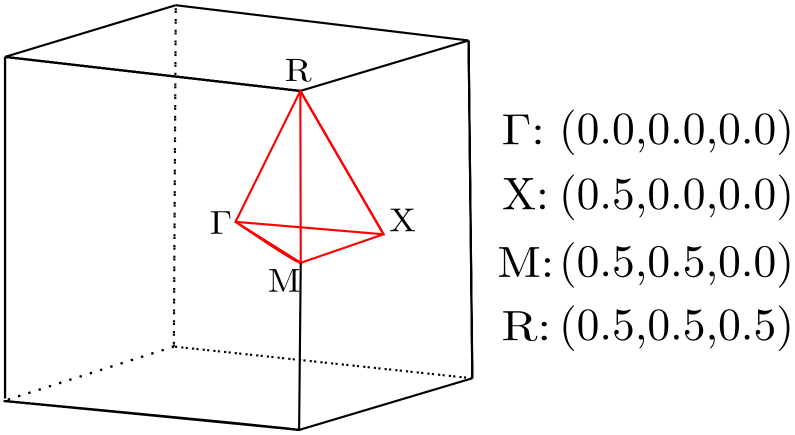

Figure S19 Brillouin zone for a cubic structure with the high-symmetry points and its coordinates.

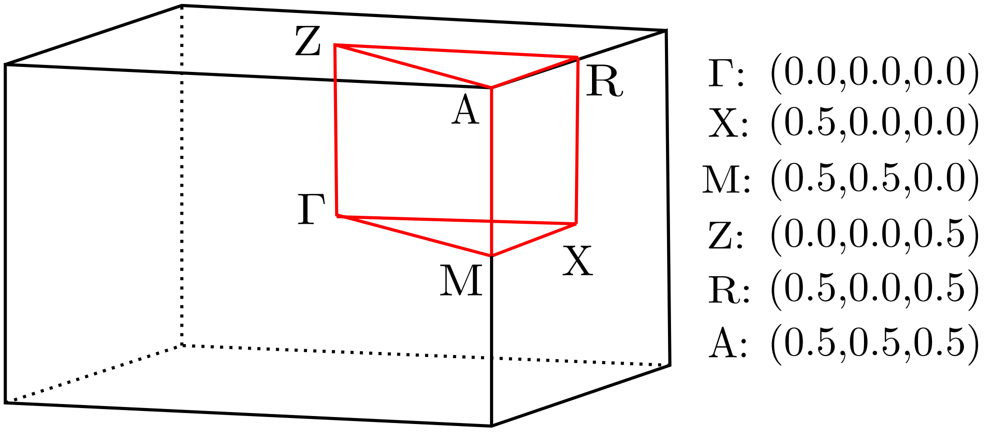

Figure S20 Brillouin zone for a tetragonal structure with the high-symmetry points and its coordinates.

On Figure S21 through Figure S29, we present the electronic band structures for 3D (left panels) and 2D (right panels) perovskites comparing the effect of SOC. The valence band maximum was shifted to 0 on each panel. Also, from Figure S30 to Figure S38, we present the same electronic band structures but on a smaller range near the band gap region.

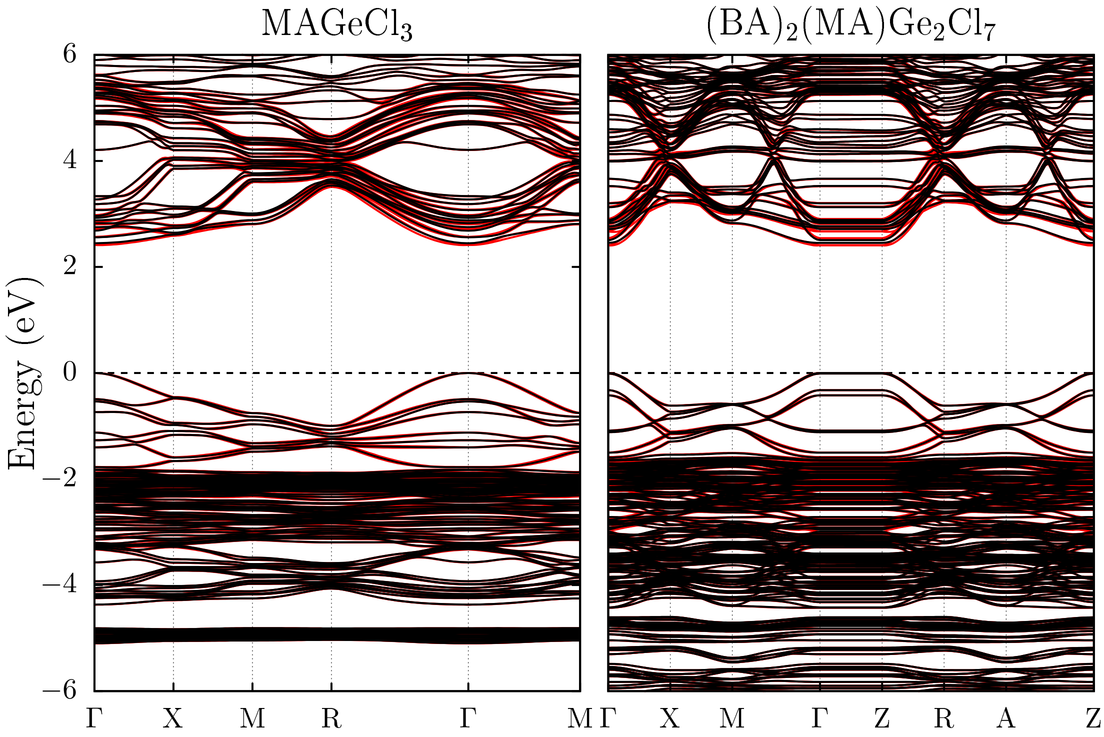

Figure S21 Electronic band structures calculated with the PBE+D3 (solid black line) and PBE+D3+SOC (solid red line) approximations for the 3D $MAGeCl_3$ and 2D $(BA)_2(MA)Ge_2Cl_7$ perovskites. The zero energy is located at the valence band maximum.

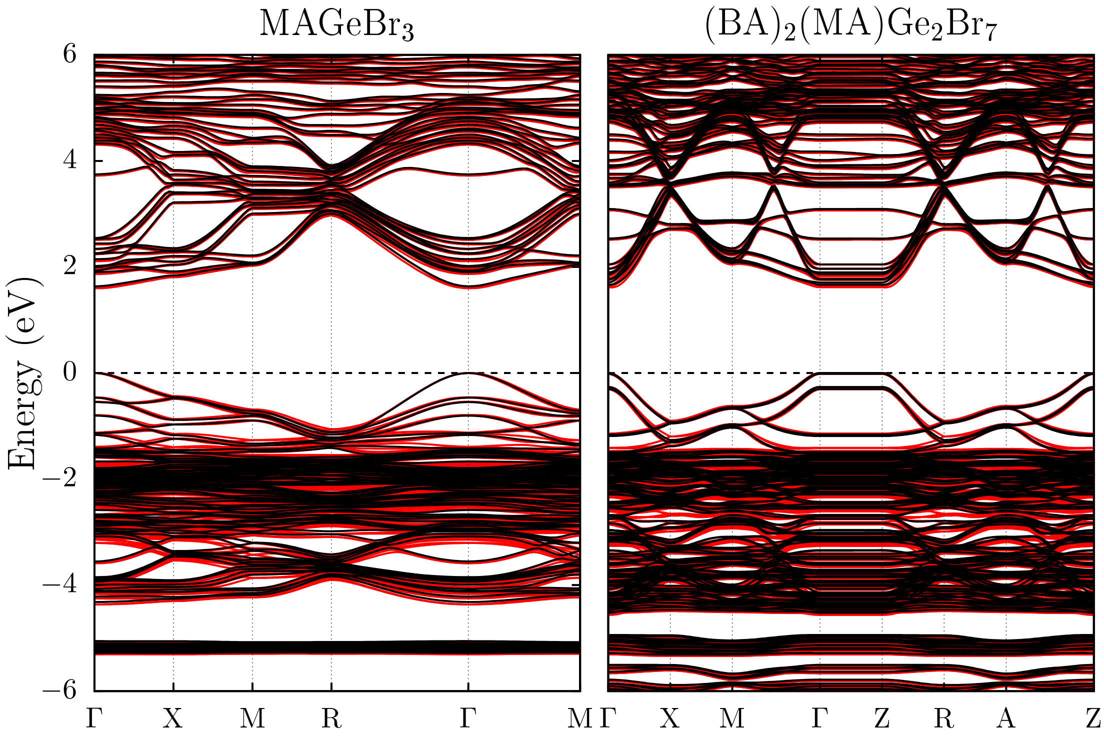

Figure S22 Electronic band structures calculated with the PBE+D3 (solid black line) and PBE+D3+SOC (solid red line) approximations for the 3D MAGeBr$_3$ and 2D (BA)$_2$(MA)Ge$_2$Br$_7$ perovskites. The zero energy is located at the valence band maximum.

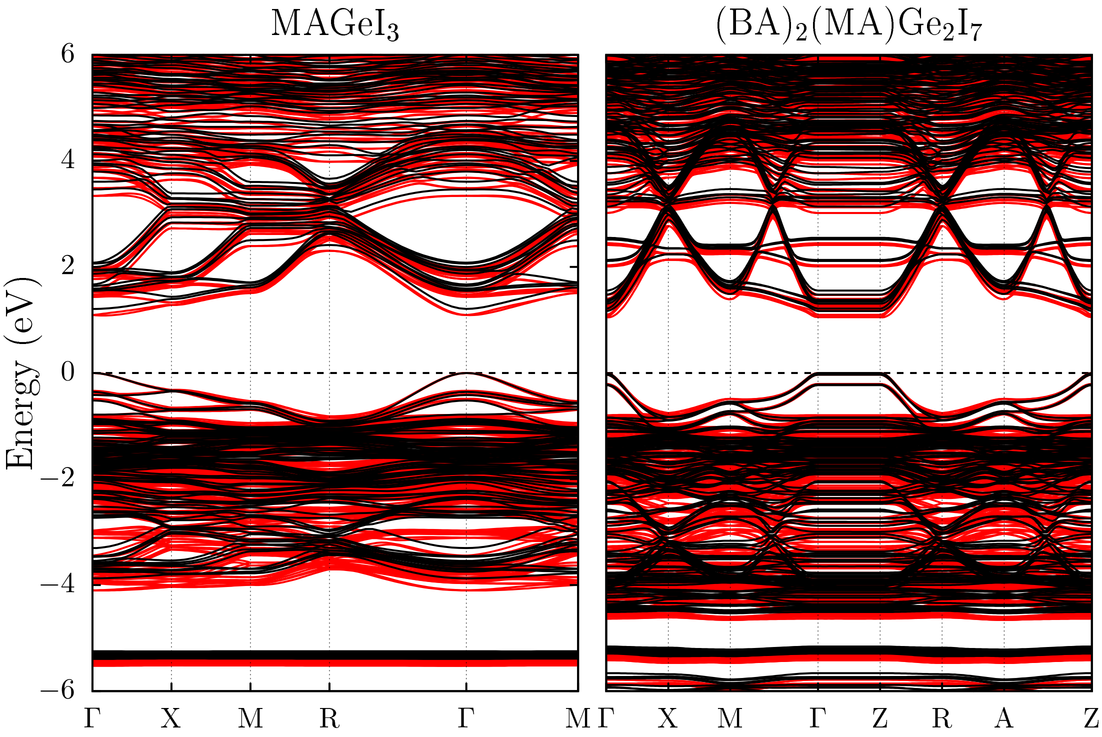

Figure S23 Electronic band structures calculated with the PBE+D3 (solid black line) and PBE+D3+SOC (solid red line) approximations for the 3D MAGeI$_3$ and 2D (BA)$_2$(MA)Ge$_2$I$_7$ perovskites. The zero energy is located at the valence band maximum.

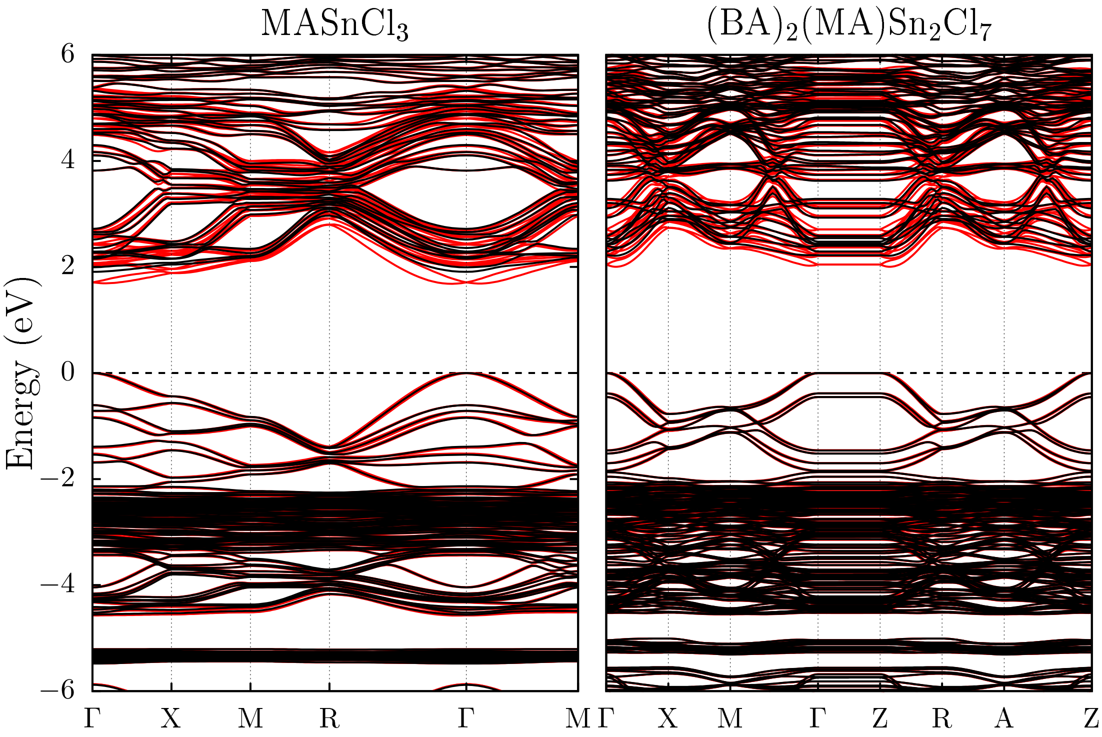

Figure S24 Electronic band structures calculated with the PBE+D3 (solid black line) and PBE+D3+SOC (solid red line) approximations for the 3D MASnCl$_3$ and 2D (BA)$_2$(MA)Sn$_2$Cl$_7$ perovskites. The zero energy is located at the valence band maximum.

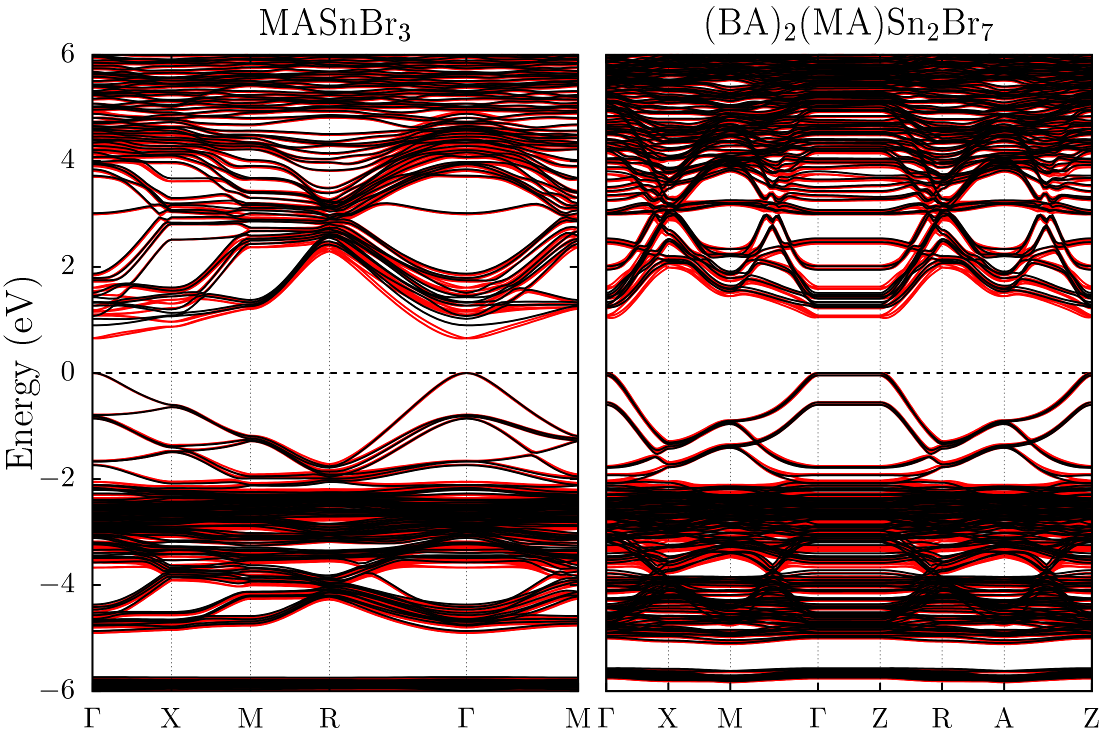

Figure S25 Electronic band structures calculated with the PBE+D3 (solid black line) and PBE+D3+SOC (solid red line) approximations for the 3D $MASnBr_3$ and 2D $(BA)_2(MA)Sn_2Br_7$ perovskites. The zero energy is located at the valence band maximum.

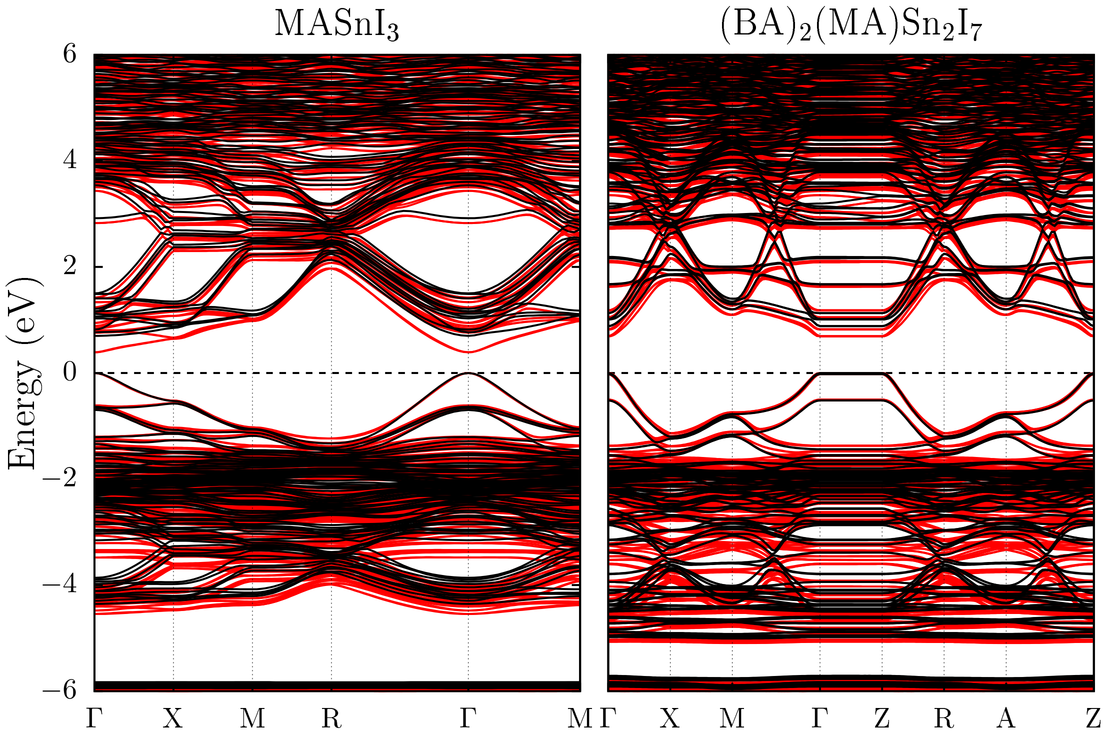

Figure S26 Electronic band structures calculated with the PBE+D3 (solid black line) and PBE+D3+SOC (solid red line) approximations for the 3D MASnI$_3$ and 2D (BA)$_2$(MA)Sn$_2$I$_7$ perovskites. The zero energy is located at the valence band maximum.

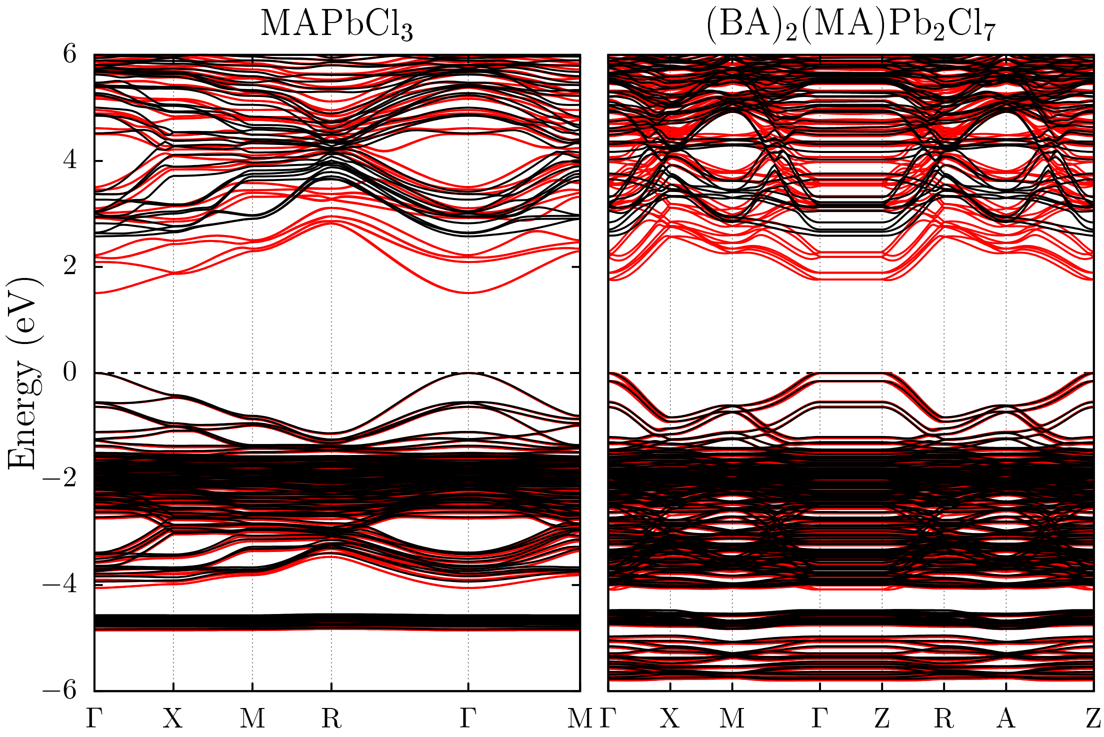

Figure S27 Electronic band structures calculated with the PBE+D3 (solid black line) and PBE+D3+SOC (solid red line) approximations for the 3D MAPbCl$_3$ and 2D (BA)$_2$(MA)Pb$_2$Cl$_7$ perovskites. The zero energy is located at the valence band maximum.

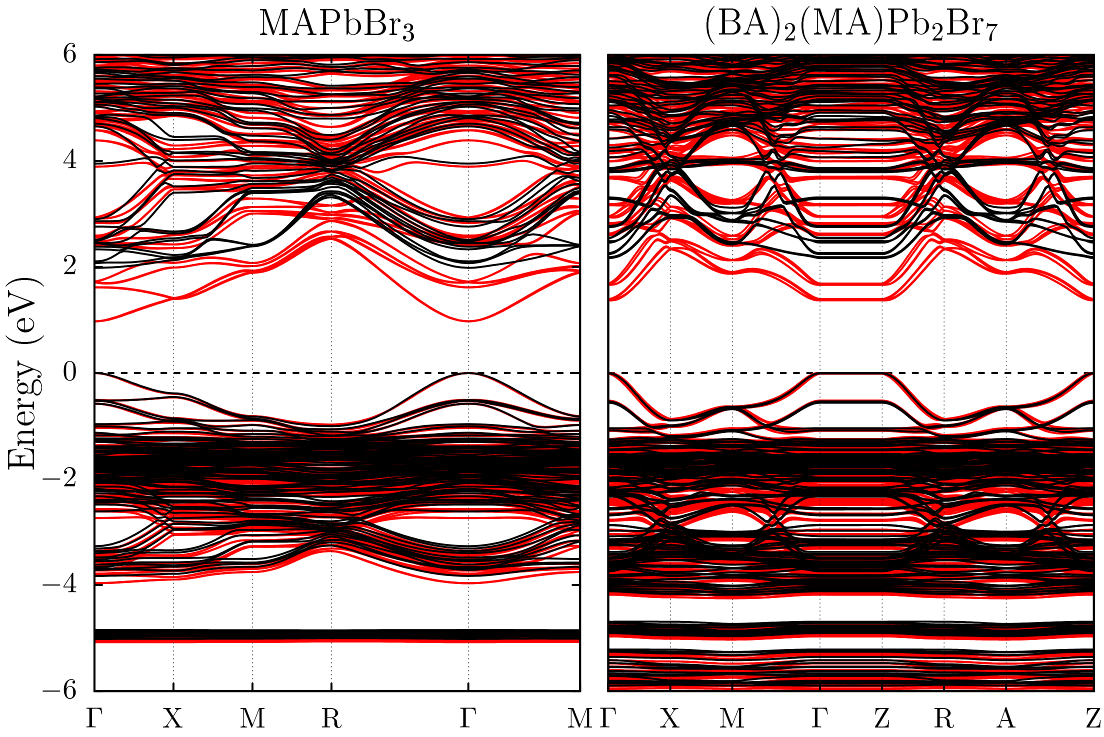

Figure S28 Electronic band structures calculated with the PBE+D3 (solid black line) and PBE+D3+SOC (solid red line) approximations for the 3D MAPbBr$_3$ and 2D (BA)$_2$(MA)Pb$_2$Br$_7$ perovskites. The zero energy is located at the valence band maximum.

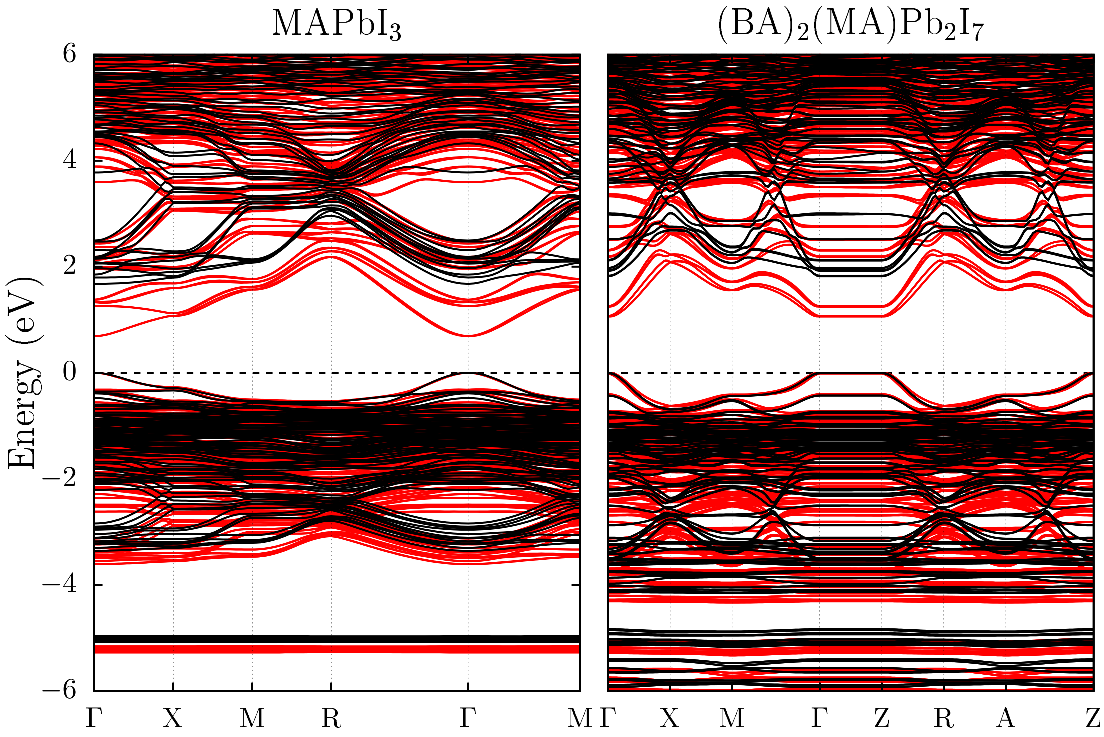

Figure S29 Electronic band structures calculated with the PBE+D3 (solid black line) and PBE+D3+SOC (solid red line) approximations for the 3D MAPbI$_3$ and 2D (BA)$_2$(MA)Pb$_2$I$_7$ perovskites. The zero energy is located at the valence band maximum.

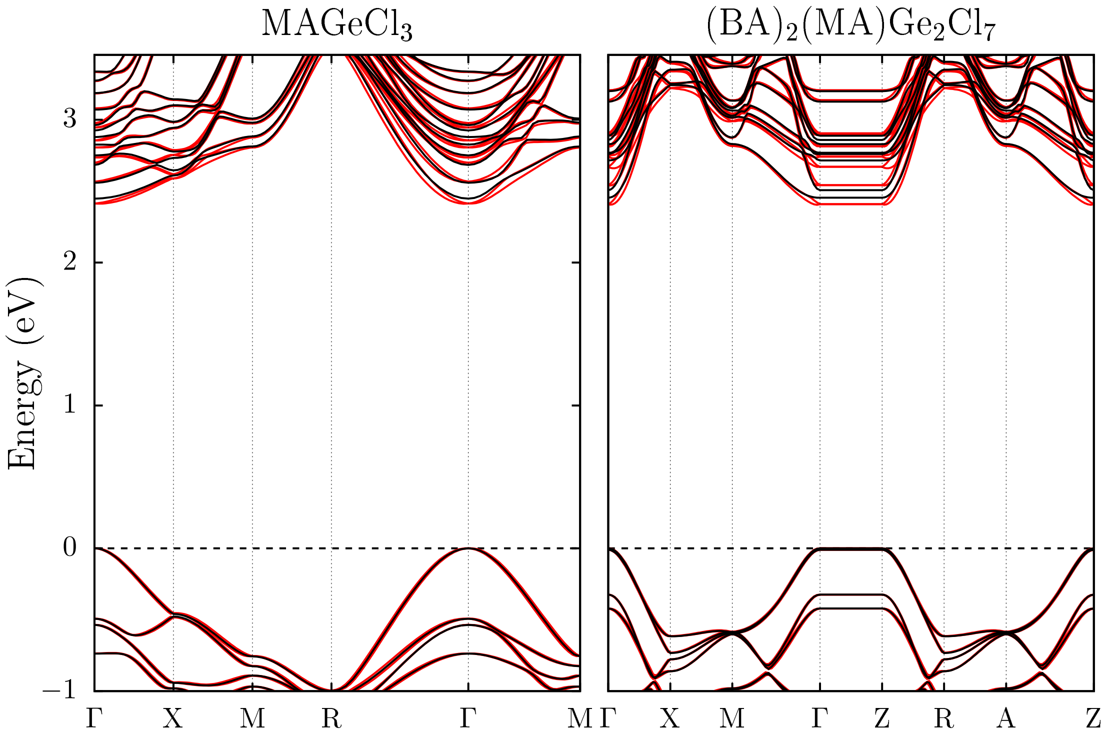

Figure S30 Electronic band structures calculated near the band gap region with the PBE+D3 (solid black line) and PBE+D3+SOC (solid red line) approximations for the 3D MAGeCl$_3$ and 2D (BA)$_2$(MA)Ge$_2$Cl$_7$ perovskites. The zero energy is located at the valence band maximum.

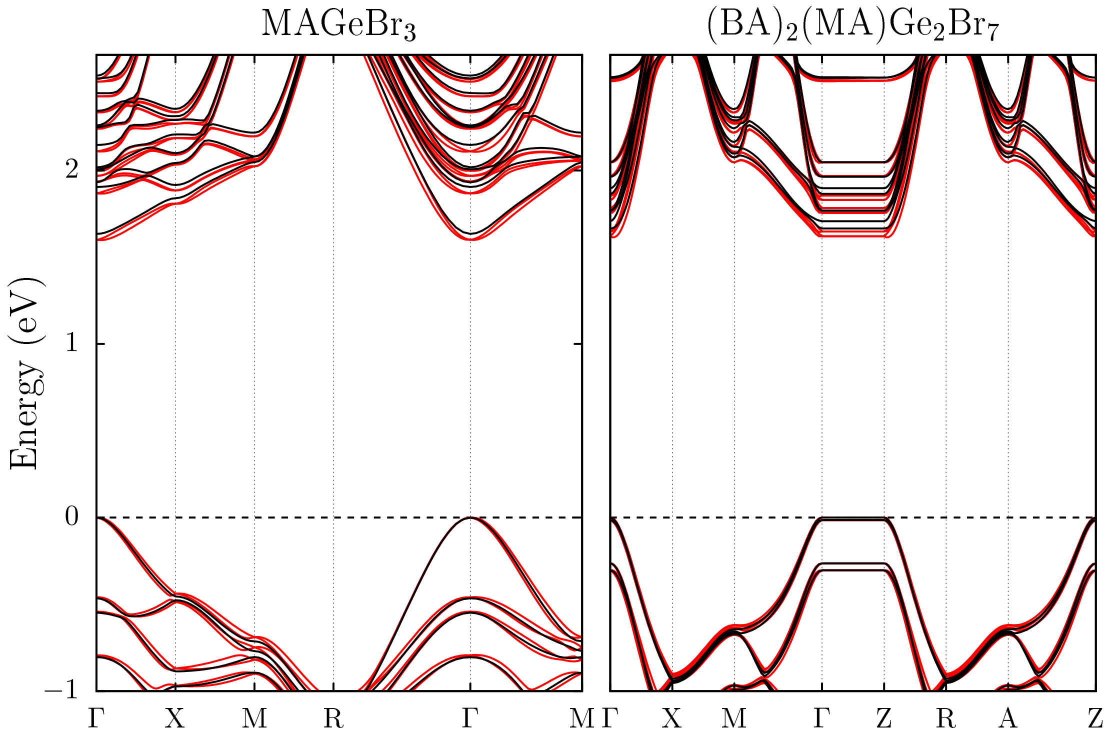

Figure S31 Electronic band structures calculated near the band gap region with the PBE+D3 (solid black line) and PBE+D3+SOC (solid red line) approximations for the 3D MAGeBr$_3$ and 2D (BA)$_2$(MA)Ge$_2$Br$_7$ perovskites. The zero energy is located at the valence band maximum.

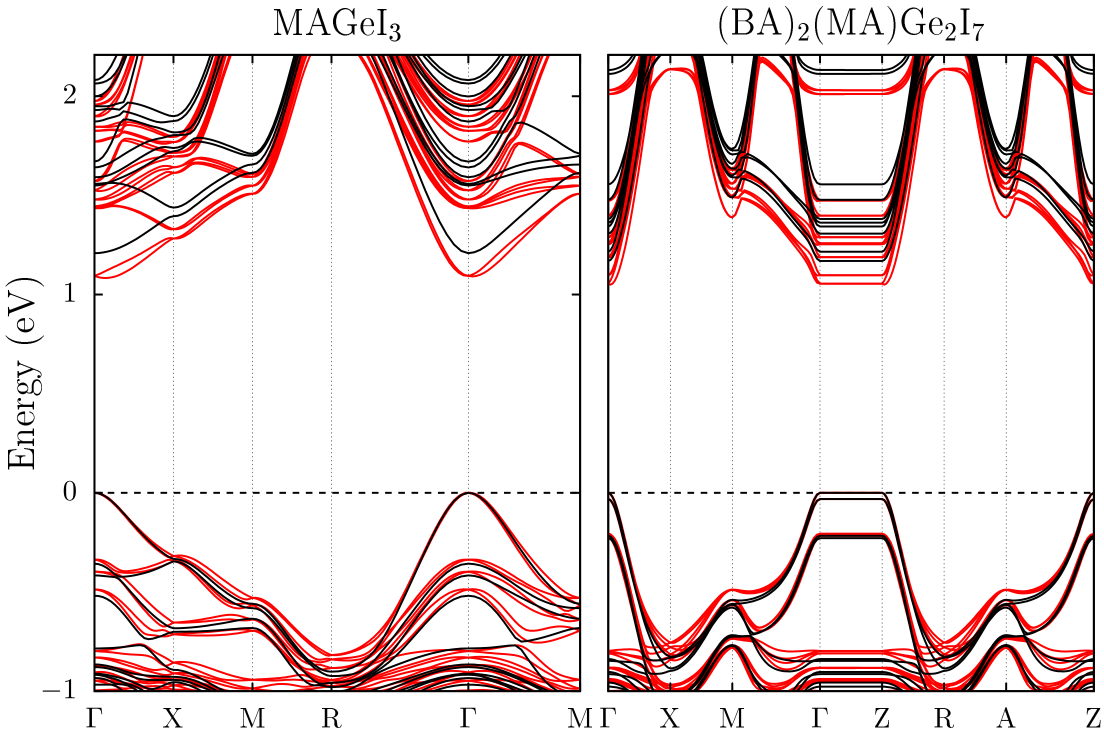

Figure S32 Electronic band structures calculated near the band gap region with the PBE+D3 (solid black line) and PBE+D3+SOC (solid red line) approximations for the 3D MAGeI$_3$ and 2D (BA)$_2$(MA)Ge$_2$I$_7$ perovskites. The zero energy is located at the valence band maximum.

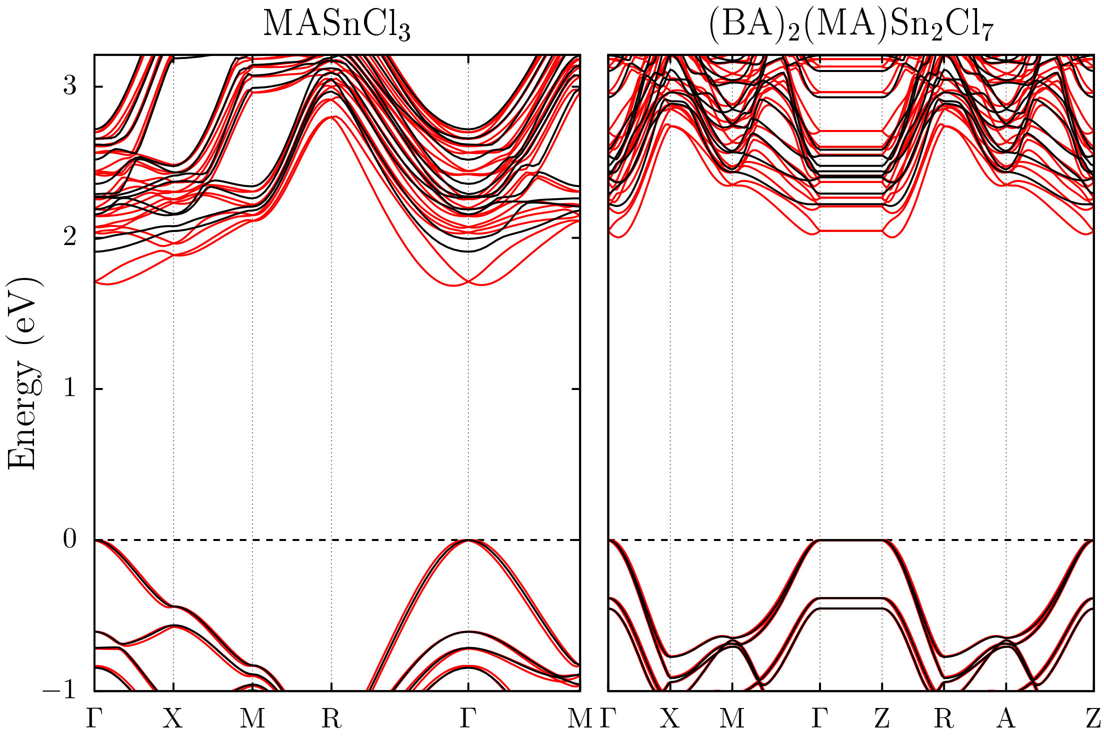

Figure S33 Electronic band structures calculated near the band gap region with the PBE+D3 (solid black line) and PBE+D3+SOC (solid red line) approximations for the 3D MASnCl$_3$ and 2D (BA)$_2$(MA)Sn$_2$Cl$_7$ perovskites. The zero energy is located at the valence band maximum.

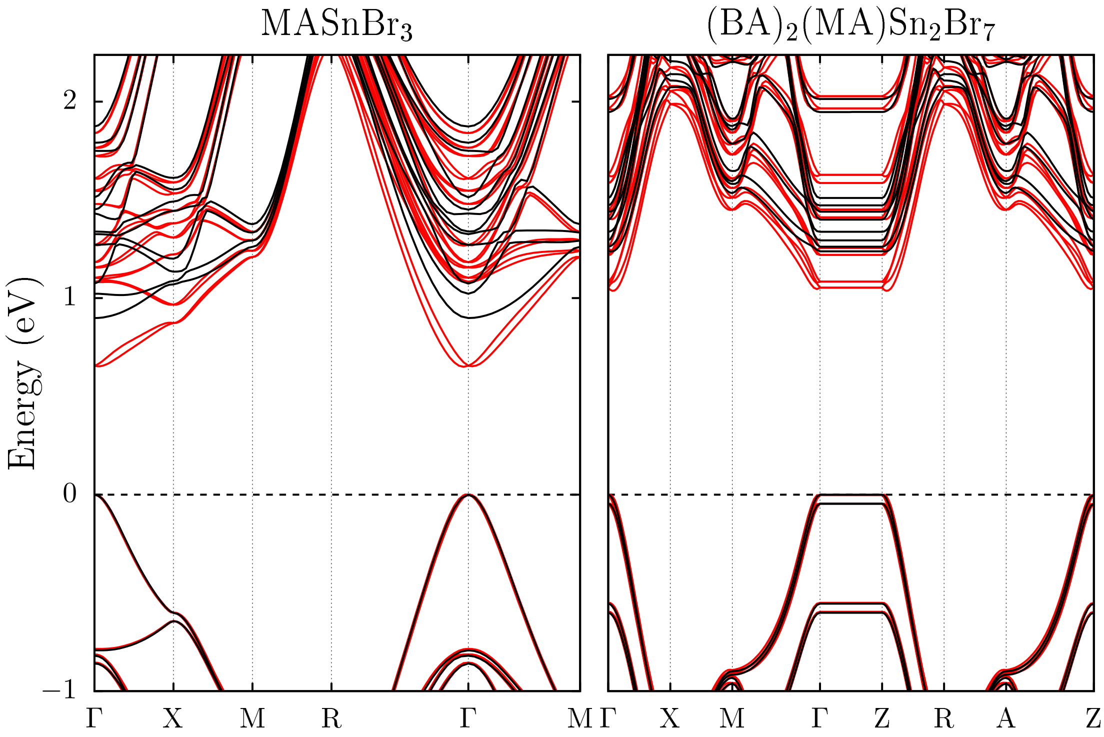

Figure S34 Electronic band structures calculated near the band gap region with the PBE+D3 (solid black line) and PBE+D3+SOC (solid red line) approximations for the 3D MASnBr$_3$ and 2D (BA)$_2$(MA)Sn$_2$Br$_7$ perovskites. The zero energy is located at the valence band maximum.

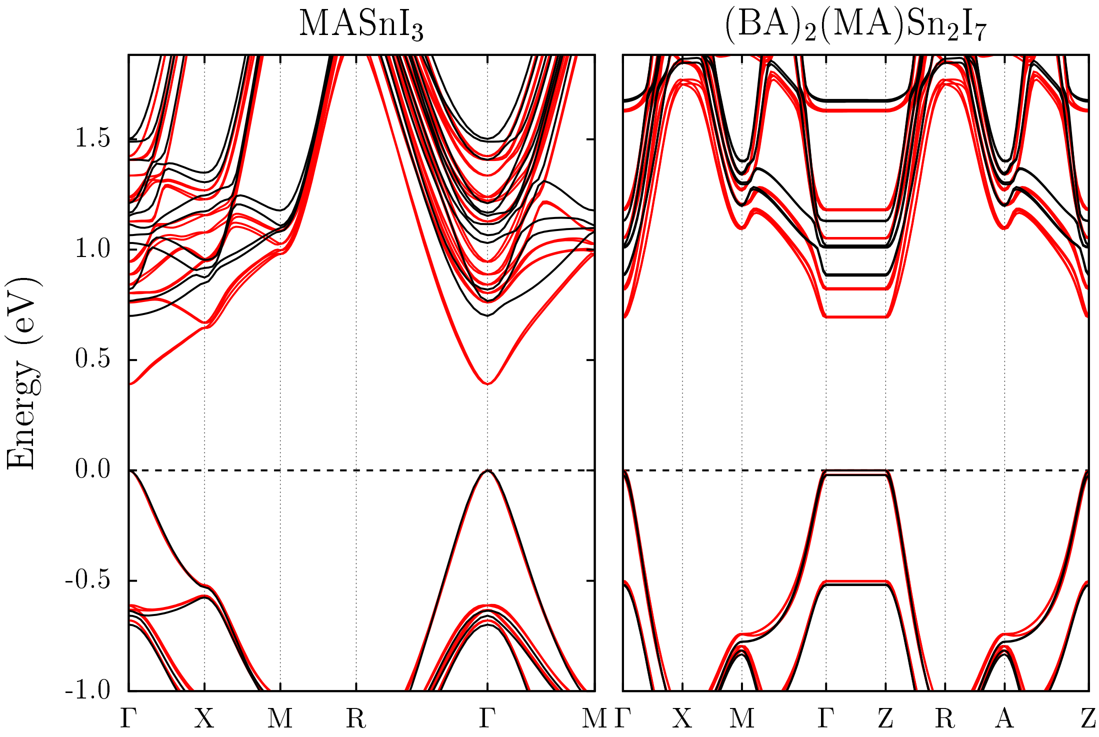

Figure S35 Electronic band structures calculated near the band gap region with the PBE+D3 (solid black line) and PBE+D3+SOC (solid red line) approximations for the 3D MASnI$_3$ and 2D (BA)$_2$(MA)Sn$_2$I$_7$ perovskites. The zero energy is located at the valence band maximum.

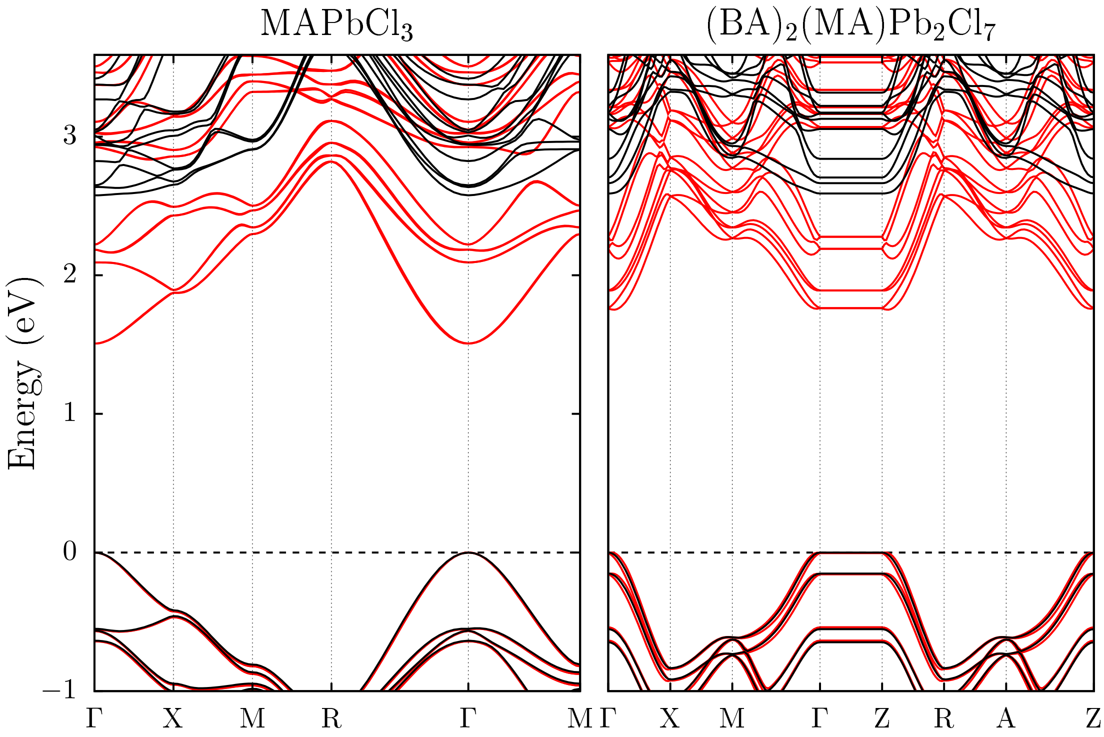

Figure S36 Electronic band structures calculated near the band gap region with the PBE+D3 (solid black line) and PBE+D3+SOC (solid red line) approximations for the 3D MAPbCl$_3$ and 2D (BA)$_2$(MA)Pb$_2$Cl$_7$ perovskites. The zero energy is located at the valence band maximum.

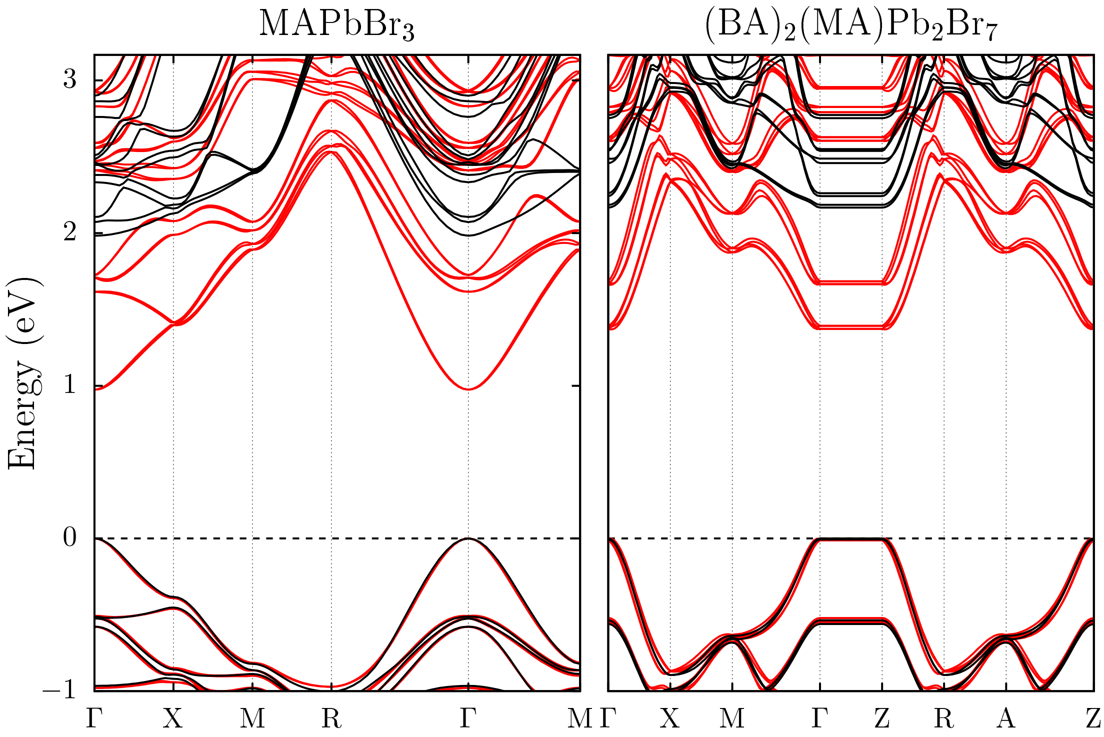

Figure S37 Electronic band structures calculated near the band gap region with the PBE+D3 (solid black line) and PBE+D3+SOC (solid red line) approximations for the 3D $MAPbBr_3$ and 2D $(BA)_2(MA)Pb_2Br_7$ perovskites. The zero energy is located at the valence band maximum.

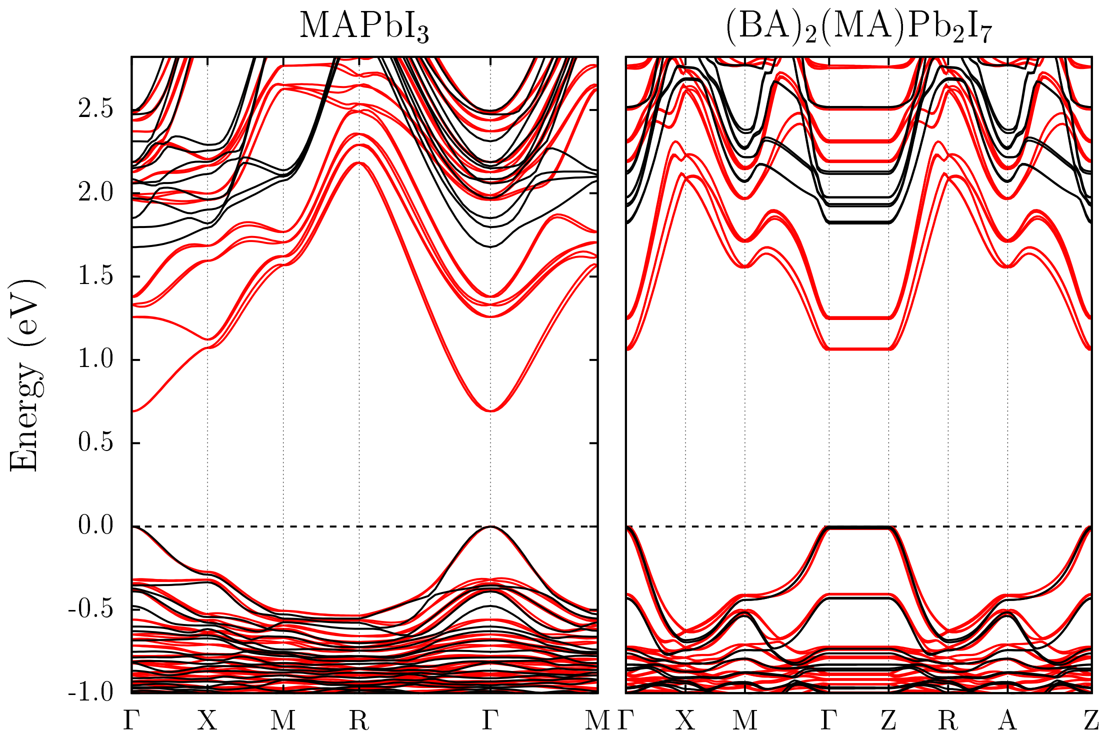

Figure S38 Electronic band structures calculated near the band gap region with the PBE+D3 (solid black line) and PBE+D3+SOC (solid red line) approximations for the 3D MAPbI$_3$ and 2D (BA)$_2$(MA)Pb$_2$I$_7$ perovskites. The zero energy is located at the valence band maximum.

11 Band Gap Corrections

Table S10 Fundamental band gap energies, in eV, for 3D and 2D perovskites calculated with different approximations, e.g., PBE+D3, PBE+D3+SOC, HSE06 (Γ-point calculation), and PBE+D3+χ (corrected by scissor operator). χ indicates the scissor operator, where $\chi = \chi^{\text{SOC}} + \chi^{\text{HSE06}}$ (differences from the PBE+D3 values). The optical band gap is also included on the last column ($E_g^{\text{op.}}$)

BX	Struct.	$\text{E}_g^{\text{PBE+D3}}$	$\text{E}_g^{\text{PBE+D3+SOC}}$	χ^{SOC}	$\text{E}_g^{\text{HSE06}}$	χ^{HSE06}	E_g	$E_g^{\text{op.}}$
GeCl	3D	2.4478	2.4122	−0.0356	3.3415	0.8937	3.3059	3.3232
	2D	2.4541	2.4047	−0.0494	3.3991	0.9450	3.3497	3.3497
GeBr	3D	1.6344	1.5984	−0.0360	2.3963	0.7619	2.3603	2.3861

Continues on next page

Table S10 – continued from previous page

BX	Struct.	$E_g^{\text{PBE+D3}}$	$E_g^{\text{PBE+D3+SOC}}$	χ^{SOC}	E_g^{HSE06}	χ^{HSE06}	E_g	$E_g^{\text{op.}}$
	2D	1.6658	1.6150	−0.0508	2.4675	0.8017	2.4166	2.4166
GeI	3D	1.2088	1.0834	−0.1254	1.7730	0.5642	1.6476	1.6792
	2D	1.1694	1.0501	−0.1193	1.7811	0.6117	1.6618	1.7398
SnCl	3D	1.9082	1.6822	−0.2260	2.6673	0.7591	2.4413	2.4851
	2D	2.2111	2.0039	−0.2072	3.0460	0.8227	2.8266	2.8266
SnBr	3D	0.8985	0.6502	−0.2483	1.5022	0.6037	1.2539	1.2539
	2D	1.2379	1.0368	−0.2011	1.9232	0.6849	1.7217	1.8124
SnI	3D	0.6997	0.3903	−0.3094	1.1930	0.4933	0.8836	0.9020
	2D	0.8822	0.6927	−0.1895	1.4182	0.5360	1.2287	1.2427
PbCl	3D	2.5765	1.5074	−1.0691	3.4064	0.8299	2.3373	2.3373
	2D	2.5898	1.7518	−0.8380	3.4745	0.8847	2.6365	2.6365
PbBr	3D	1.9829	0.9749	−1.0080	2.7110	0.7281	1.7030	1.7030
	2D	2.1672	1.3688	−0.7984	2.9479	0.7807	2.1495	2.1836
PbI	3D	1.6768	0.6910	−0.9858	2.2824	0.6056	1.2966	1.2966
	2D	1.8185	1.0596	−0.7589	2.4562	0.6377	1.6973	1.7143

On Table S10 we present the fundamental electronic band gaps obtained from PBE+D3, PBE+D3+SOC and HSE06 calculations for both 3D and 2D perovskite systems. HSE06 results are more accurate than PBE+D3 ones, but including SOC effects would greatly increase the computational costs of the simulations. Therefore, we achieved a trade-off between accuracy and simulation costs by having calculations for PBE+D3+SOC and HSE06 on Γ, and employing a scissors operator from both contributions to the PBE+D3 band gap. On the last column of Table S10 we also present the optical band gap of the systems, obtained from the first observed optical transition.

12 Absorption Coefficient

The absorption coefficient ($\alpha(\omega)$) is calculated using the following equation:

$$\alpha(\omega) = \frac{\sqrt{2}\omega}{c}\left[\sqrt{\varepsilon_R^2 + \varepsilon_I^2} - \varepsilon_R\right]^{\frac{1}{2}}, \qquad (15)$$

in which ω is the incident photon frequency, c stands for the speed of light, and the terms ε_R and ε_I are respectively the real and imaginary parts of the dielectric function. As $\varepsilon(\omega)$ is a tensor, the absorption coefficient is separable within its coordinates and we calculate the total absorption coefficient as the sum of the three diagonal components (xx, yy, zz).

References

(1) Kieslich, G.; Sun, S.; Cheetham, A. K. Solid-state Principles Applied to Organic–Inorganic Perovskites: New Tricks for an Old Dog. *Chem. Sci.* **2014**, *5*, 4712–4715, DOI: 10.1039/c4sc02211d.

(2) Shannon, R. D. Revised Effective Ionic Radii and Systematic Studies of Interatomic Distances in Halides and Chalcogenides. *Acta Crystallogr., Sect. A: Found. Crystallogr.* **1976**, *32*, 751–767, DOI: 10.1107/s0567739476001551.

(3) Chen, Q.; Marco, N. D.; Yang, Y. M.; Song, T.-B.; Chen, C.-C.; Zhao, H.; Hong, Z.; Zhou, H.; Yang, Y. Under the Spotlight: The Organic–Inorganic Hybrid Halide Perovskite for Optoelectronic Applications. *Nano Today* **2015**, *10*, 355–396, DOI: 10.1016/j.nantod.2015.04.009.

(4) Saparov, B.; Mitzi, D. B. Organic–Inorganic Perovskites: Structural Versatility for Functional Materials Design. *Chem. Rev.* **2016**, *116*, 4558–4596, DOI: 10.1021/acs.chemrev.5b00715, PMID: 27040120.

(5) Hoefler, S. F.; Trimmel, G.; Rath, T. Progress on Lead-free Metal Halide Perovskites for Photovoltaic Applications: A Review. *Monatsh. Chem.* **2017**, *148*, 795–826, DOI: 10.1007/s00706-017-1933-9.

(6) Stoumpos, C. C.; Cao, D. H.; Clark, D. J.; Young, J.; Rondinelli, J. M.; Jang, J. I.; Hupp, J. T.; Kanatzidis, M. G. Ruddlesden–Popper Hybrid Lead Iodide Perovskite 2D Homologous Semiconductors. *Chem. Mater.* **2016**, *28*, 2852–2867, DOI: 10.1021/acs.chemmater.6b00847.

(7) Zhao, X.-G.; Dalpian, G. M.; Wang, Z.; Zunger, A. Polymorphous Nature of Cubic Halide Perovskites. *Phys. Rev. B* **2020**, *101*, 155137, DOI: 10.1103/physrevb.101.155137.

(8) Dias, A. C.; Lima, M. P.; Da Silva, J. L. F. Role of Structural Phases and Octahedra Distortions in the Optoelectronic and Excitonic Properties of CsGeX_3 (X = Cl, Br, I) Perovskites. *J. Phys. Chem. C* **2021**, *125*, 19142–19155, DOI: 10.1021/acs.jpcc.1c05245.

(9) Momma, K.; Izumi, F. VESTA: A Three-Dimensional Visualization System for Electronic and Structural Analysis. *J. Appl. Cryst.* **2008**, *41*, 653–658, DOI: 10.1107/s0021889808012016.

(10) Henkelman, G.; Arnaldsson, A.; Jónsson, H. A Fast and Robust Algorithm for Bader Decomposition of Charge Density. *Comput. Mater. Sci.* **2006**, *36*, 354–360, DOI: 10.1016/j.commatsci.2005.04.010.